

Computational Analysis of Sweeping Jet Actuator  
using Dynamic Mode Decomposition

By

MOBASHERA ALAM  
Bachelor of Science in Mechanical Engineering.  
Bangladesh University of Engineering and Technology  
Dhaka, Bangladesh  
2019

Submitted to the Faculty of the  
Graduate College of  
Oklahoma State University  
in partial fulfillment of  
the requirements for  
the Degree of  
MASTER OF SCIENCE  
December, 2022

Computational Analysis of Sweeping Jet Actuator  
using Dynamic Mode Decomposition

Thesis Approved:

Dr.Kursat Kara

---

Thesis Advisor

Dr.Omer San

---

Dr.Aaron Alexander

---

## ACKNOWLEDGMENTS

In the name of Almighty for giving me the strength to come so far at the end of my Master of Science graduation. I would like to express my utmost gratitude to my advisor Dr. Kursat Kara for his constant support, guidance, patience and encouragement. I want to sincerely thank Dr. Omer San and Dr. Aaron Alexander for being part of my graduation journey. Finally, I am grateful to my parents for their constant support and inspiration to help me grow as I am today.

Acknowledgments reflect the views of the author and are not endorsed by committee members or Oklahoma State University.

*“If your dreams don’t scare you, they are too small.”*

*—Richard Branson*

*This thesis book is dedicated to my mom for inspiring me to be who I am  
today.*

Acknowledgements reflect the views of the author and are not endorsed by committee members or Oklahoma State University.

Name: MOBASHERA ALAM

Date of Degree: December, 2022

Title of Study: COMPUTATIONAL ANALYSIS OF SWEEPING JET ACTUATOR  
USING DYNAMIC MODE DECOMPOSITION

Major Field: MECHANICAL AND AEROSPACE ENGINEERING

Abstract: A sweeping jet actuator (SJA) is a self-sustaining, periodically oscillating device without involving any moving parts. SJA requires only pressurized fluid at the inlet to transfer momentum via the Coanda effect. As an active flow control device, SJA is a reliable option for suppressing aerodynamic flow separation. SJAs are integrated into series which eject bi-stable harmonic oscillation to suppress the separation bubble created downstream of the aerodynamic components. In this thesis, we analyzed the geometric variations of the SJA to combine with aerodynamic wings, and stabilizers using computational fluid dynamics (CFD). Based on high-fidelity CFD data, we further developed a reduced order model (ROM) using dynamic mode decomposition (DMD). The ROM solutions have been demonstrated to be successful in decreasing computational costs greatly with negligible loss in physical accuracy and therefore a proven alternative to existing methodologies for cost reduction. DMD algorithm provides the output of the SJA device that can be utilized as a boundary condition to decrease the numerical burden of simulating micro-scale structure in macro-scale models.

## TABLE OF CONTENTS

Chapter	Page
<b>I Introduction</b> . . . . .	<b>1</b>
1.1 Motivation . . . . .	1
1.2 Literature Survey . . . . .	2
<b>II The Influence of Exit Nozzle Geometry on Sweeping Jet Actuator</b>	<b>13</b>
2.1 Overview . . . . .	13
2.2 Introduction . . . . .	14
2.3 Numerical Setup and Geometric Details . . . . .	16
2.4 Governing Equations . . . . .	17
2.4.1 Computational Fluid Dynamics Model . . . . .	20
2.5 Mesh Independence Test . . . . .	20
2.6 Model Validation and Verification . . . . .	24
2.7 Results and Discussion . . . . .	25
2.7.1 Effect of Curvature . . . . .	26
2.7.2 Effect of Exit Nozzle Angle . . . . .	30
2.7.3 Effect of Length: Both Nozzle Arms . . . . .	30
2.7.4 Effect of Length: Top Nozzle Arm (Asymmetry) . . . . .	33
2.8 Discussion . . . . .	34
<b>III Analysis of High-Frequency Jet Oscillation using Dynamic Mode Decomposition with Eigenvalue-Based Selection Algorithm</b> . . . . .	<b>36</b>
3.1 Overview . . . . .	36
3.2 Introduction . . . . .	37
3.3 Methodology . . . . .	40
3.3.1 DMD Outline . . . . .	41
3.3.2 Selection of DMD Modes . . . . .	46
3.3.2.1 Sorting Criteria-1:Based on Amplitude . . . . .	49
3.3.2.2 Sorting Criteria-2:Based on Growth/Decay Rate . . . . .	49
3.3.2.3 Sorting Criteria-3:Based on Amplitude with Time . . . . .	50
3.3.2.4 Sorting Criteria-4: Based on Eigenvalues . . . . .	50
3.3.3 Results . . . . .	53
3.3.3.1 Sensitivity Analysis for Time Step . . . . .	58
3.3.3.2 Sensitivity Analysis for Number of Dominant Modes . . . . .	60
3.3.3.3 Sensitivity Analysis for Oscillation Frequency . . . . .	68
3.4 Conclusion . . . . .	70
<b>IV Remarks</b> . . . . .	<b>71</b>
4.1 Summary . . . . .	71
4.2 Limitations and Future Work . . . . .	73

Chapter	Page
References . . . . .	74

## LIST OF TABLES

Table		Page
2.1	Mesh details for computation. . . . .	21
2.2	Model validation and verification. . . . .	25
2.3	Oscillation frequency for different cases at the upper and lower feed-back channel. . . . .	26



## LIST OF FIGURES

Figure		Page
1.1	(a) Working principle of Sweeping Jet Actuator [1], (b) Velocity distribution of actuator field [2]. . . . .	4
1.2	Sweeping Jet Actuators integrated at the leading edge of NASA Trap Wing for flow control [3]. (Part of this image is adapted from [4]) . .	8
1.3	Flow control with sweeping jet actuator in NASA hump model[5]. . .	12
1.4	Geometric variation analysis on exit nozzle of sweeping jet actuator for flexible integration [6]. . . . .	12
2.1	Computational domain of the SJA and the flow field (baseline). . . .	17
2.2	Schematic diagram of the sweeping jet actuator including the tested geometric parameters of the exit nozzle, <b>(a)</b> angle, where $\theta =$ half exit nozzle angle, <b>(b)</b> top arm length variation, L-top, <b>(c)</b> both arm lengths' variation, L-both, and <b>(d)</b> curvature, where L = nozzle length. . . .	18
2.3	<b>(Left)</b> SJA geometry showing the position of different sampling points, uf, lf, and x6y0, exit nozzle height, h, exit nozzle length,l and (red circle) used for focused meshing. <b>(Right)</b> Close view of the mesh near the exit nozzle. . . . .	22
2.4	<b>(a)</b> Time history at (P-uf), (P-lf), and (P-x6y0) showing the pressure amplitude for N-60 and corresponding FFT analysis <b>(b)</b> at those sampling locations where peaks indicate the oscillation frequency. . . . .	22
2.5	Oscillation frequency obtained from FFT analysis for 0.1s at different sampling points based on the velocity magnitude (v) and static pressure (p): downstream, x6y0 (6 mm, 0 mm), upper feedback channel, uf (-25.4 mm, 19 mm), and lower feedback channel, lf (-25.4 mm, -19 mm), for different mesh distributions. . . . .	23
2.6	Local error analysis of the mean pressure along the centerline based on the finest (N-80) mesh. The mean pressure is normalized by the inlet $P_{in} = 128,961.46$ Pa. . . . .	24
2.7	Local error analysis of the mean velocity along the centerline based on the finest (N-80) mesh. The mean velocity is normalized by the inlet mean velocity $V_{in} = 44.83$ m/s. . . . .	24
2.8	<b>(I)</b> Mean velocity along the centerline normalized by the inlet velocity, $V_{in,Baseline}$ ; <b>(II)</b> velocity ratio, $\eta$ at point $x/h = 5$ . . . . .	29
2.9	At $x/h = 5$ , <b>(a)</b> half-jet width for curvature, L-top and L-both cases (in terms of nozzle length, $x/h$ ) and angle case (in terms of the half-exit angle, $\theta$ ). <b>(b)</b> Velocity profile for the curvature case. . . . .	31

Figure	Page
2.10 Instantaneous total pressure along the centerline normalized with the total inlet pressure, $P_{total,Baseline} = 131,829.66$ Pa for curvature cases.	32
2.11 Mean pressure along the centerline normalized by inlet, $P_{in,Baseline}$ for (a) Angle, (b) Curvature, (c) L-both and (d) L-top. . . . .	33
3.1 Outline for the dimensionally-reduced spatio-temporal system analysis using sorted DMD algorithm and its application. . . . .	40
3.2 DMD Flow Chart . . . . .	42
3.3 Working principle of different DMD sorting criteria based on modes, $N = 150$ for system frequency, $f = 131.75\text{Hz}$ . . . . .	48
3.4 Corresponding eigen values of the chosen modes, $N = 150$ for system frequency, $f = 131.75\text{Hz}$ and time-step, $\Delta t = 5 \times 10^{-5}\text{s}$ for four sorting.	52
3.5 First 4 discrete dominant modes of our proposed sorting criteria-4 showing the coherent pattern of the flow. . . . .	53
3.6 Comparison between CFD and DMD result for s1 at the center point (0,0) data for (a) $\Delta t=2 \times 10^{-5}\text{s}$ , (b) $\Delta t=5 \times 10^{-5}\text{s}$ , (c) $\Delta t= 10^{-4}\text{s}$ for system frequency, $f = 131.75\text{Hz}$ and modes, $N = 150$ . $u^*$ and $t^*$ are normalized velocity and time period. . . . .	56
3.7 Comparison between CFD and DMD result for S4 at the center point (0,0) data for (a) $\Delta t=2 \times 10^{-5}\text{s}$ , (b) $\Delta t=5 \times 10^{-5}\text{s}$ , (c) $\Delta t= 10^{-4}\text{s}$ . $u^*$ and $t^*$ are normalized velocity and time period. . . . .	57
3.8 Root mean square error(RMSE) of the nozzle exit window using: s1 and s4 with studied time step $\Delta t_1 = 2 \times 10^{-5}\text{s}$ , $\Delta t_2 = 5 \times 10^{-5}\text{s}$ , $\Delta t_3 = 10^{-4}\text{s}$ , mass flow rate, $\dot{m} = 0.005\text{lb/s}$ ,mode number, $N = 150$ . . .	60
3.9 Velocity probe (0,0), 6 period of reconstruction s1 (S1) and s4 (S4) for $\dot{m} = 0.005\text{lb/s}$ , $\Delta t= 5 \times 10^{-5}\text{s}$ , $N = 150$ . $u^*$ and $t^*$ are normalized velocity and time period. . . . .	62
3.10 Pressure sub-sampling at center point (0,0), 6 periods of reconstruction s1 and s4 for $\dot{m} = 0.005\text{lb/s}$ , $\Delta t= 5 \times 10^{-5}\text{s}$ , $N = 150$ . $P^*$ and $t^*$ are normalized total pressure and time period. . . . .	63
3.11 Velocity sub-sampling at center point (0,0), 6 periods of reconstruction and another 6 periods of prediction with sorting-1 (S1) and sorting-4 (S4) for $\dot{m} = 0.005\text{lb/s}$ , $\Delta t= 5 \times 10^{-5}\text{s}$ , $N = 250$ . . . . .	64
3.12 Pressure probe at (0,0), 6 periods of reconstruction and 6 periods of prediction with s1 (S1) and s4 (S4) for $\dot{m} = 0.005\text{lb/s}$ , $\Delta t= 5 \times 10^{-5}\text{s}$ , $N = 250$ . . . . .	65
3.13 Pressure probe at (0,0) for low rank,m construction with s4: (a) $N=5$ , (b) $N=10$ , (c) $N=20$ for mass flow rate, $\dot{m}=0.005\text{lb/s}$ , $\Delta t= 5 \times 10^{-5}\text{s}$ .	66
3.14 u-velocity at centerpoint (0,0) for low rank(modes,m) construction with s4: (a) $N=5$ , (b) $N=10$ , (c) $N=20$ . . . . .	67
3.15 Point sampling (0,0) for u-velocity showing the reconstruction and prediction capability for (a) $\dot{m}_1=0.0025\text{lb/s}$ , $\Delta t= 2 \times 10^{-5}\text{s}$ and (b) $\dot{m}_3=0.01\text{lb/s}$ , $\Delta t=10^{-4}\text{s}$ using s4. . . . .	69

## ABBREVIATIONS

SJA	Sweeping Jet Actuator
ES-DMD	Eigen-Value Based Sorted Dynamic Mode Decomposition
CFD	Computational Fluid Dynamics
SVD	Singular Value Decomposition
SST	Shear Stress Transport
ROM	Reduced Order Modelling
POD	Proper Orthogonal Decomposition
PIV	Particle Image Velocimetry
2D	Two Dimensional
CEC	Cumulative Energy Content
RMSE	Root Mean Square Error

## NOMENCLATURE

VARIABLES	UNITS	DESCRIPTION
$v$	m/s	Velocity
$P$	Pa	Total Pressure
$T$	k	Temperature
$h$	J/kg	Specific Enthalpy
$e$	J/kg	Specific Energy
$q$	W/m <sup>2</sup>	Heat Flux
$t$	s	Time
$\dot{m}$	kg/s	Mass Flow Rate

GREEK SYMBOLS	UNITS	DESCRIPTION
$\rho$	kg/m <sup>3</sup>	Density
$\mu$	Pa s	Molecular Viscosity
$\omega$		Eigenvector
$\Lambda$		Eigenvalues
$\Phi$		Dominant Modes
$\sigma$		Singular Values

# CHAPTER I

## Introduction

### 1.1 Motivation

When pressurized with a fluid, the sweeping jet actuator (SJA) emits a self-induced and self-sustained temporally continuous, but spatially oscillating bi-stable jet at the outlet. The SJA adds up local momentum using the Coanda extension without any moving parts and, therefore, can be a promising tool for suppressing aerodynamic flow separation. However, the SJA needs to be integrated into curved aerodynamic surfaces with an angle. The present study focuses on investigating the effects of various exit nozzle geometries on the flow field. The geometric parameters considered were the exit nozzle angle, diffuser arm length, and curvature. The working fluid was air, and the mass flow rate was 6.8 g/s. A set of time-dependent flow fields was computed using a two-dimensional unsteady Reynolds-averaged Navier–Stokes (URANS) simulation. The time history of pressure was recorded inside the upper and lower feedback channels. The jet oscillation frequency was obtained by employing the fast Fourier transform (FFT) for all dataset. The results were compared against the baseline case and data available in the literature. The results showed that external geometric variations at the nozzle exit had a negligible impact on the oscillation frequency. However, there were notable effects on the pressure and velocity distribution in the flow field, indicating that the actuator had sensitivity towards the geometric variation of the exit nozzle—the wider the exit nozzle, the lower the downstream velocity. Notably, we observed that the mean velocity at the exit nozzle downstream for the curvature case was 40.3% higher than the reference SJA.

The flow field of SJA is governed by complex non-linear time-dependent Navier-Stokes equations computationally expensive to solve using high-rank computational fluid dynamics (CFD). The dynamic mode decomposition (DMD) algorithm can capture the oscillating behavior of complex flow structures by identifying the low-rank coherent structures and superimposing the dominant modes to reconstruct the system. With spectral decomposition, the DMD can identify the dominant patterns in the time-sensitive oscillating flow structure - making it a valuable tool for resolving spatio-temporal behavior. The algorithm requires specific criteria for selecting the DMD modes to reduce the system's order to obtain the recurrent pattern with high accuracy. We proposed an eigenvalue-based sorting dynamic mode decomposition (ES-DMD) algorithm along with time-delay embedding in this thesis. We considered velocity and pressure data in a two-dimensional SJA flow field for validation. Moreover, we investigated the optimum time step and the sorting method of dominant modes for reconstructing and predicting the coherent structure for various mass flow rates. Finally, we obtained a time-dependent boundary condition of velocity and pressure profiles by adding time-delay embedding to compensate for insufficient spatial data. Using the proposed approach, we recovered 90% of the flow field using less than 20% of the modes. This approach can reduce the computational cost of high frequency multi-scale simulations.

The thesis concludes with a discussion about the limitations of the developed technique, and further extensions of the technique are proposed, along with the possible approaches to achieve them.

## 1.2 Literature Survey

Fluidic oscillator has been studied experimentally to understand the flow physics better as well as to develop a numerical model. Preliminary design of fluidic oscillator contains two different inlets through which fluids enters into the mixing chamber to

create the oscillating frequency. Pressure sensitive paint (PSP) is used for visualizing the flow distribution of oscillator [7]. Another study [8] termed this as "feedback-free oscillator" and worked on observing the performance of fluidic oscillator due to dimensional variation to check the optimal operating range. The result shows fluctuating behaviour of oscillator with the change of aspect ratio, size, fluid-type. Extension of this work experimented the performance of fluidic oscillator at lower flow rate (below 3.4 mL/s) [9]. The result shows that both of the jets bifurcate each other without completely cutting off. Raghu et al. [1] focused on different methods to produce sweeping jets along with frequencies, flow rates starting from the history and later discussed on the modified version of the fluidic oscillator with feed-back channels with a single inlet and two different outlet for producing pulsing jet which is known as, 'Angled Oscillator' making the fluidic oscillator more suitable for low mass flow rate. In Kara et al. [5] a numerical model is developed on analyzing the efficiency of SJA actuator to control the flow separation through active flow control. Two-dimensional (2D) unsteady Reynold's Averaged Navier Stokes (URANS) model is used in a wall-mounted hump model with the actuator integrated in an inclined direction. Another article of Kara et al. [2] based on the 3D model of URANS analyzed the internal and external flow for a variety of mass flow rate and they determined pressure drop and the effect on jet oscillation. The computational analysis is validated with several experimental and numerically data that are previously obtained, by varying geometry, type, and working fluid accordingly. A computational study for characterization of the jet oscillation of actuator is conducted by Furkan et al.[10] by varying the mass flow rate from incompressible to subsonic compressible flow. This 3D URANS model is proven to be a cost-effective alternative for SJA performance analysis. An important finding is the constant Strouhal number(inferring a stable oscillating flow mechanism) for the oscillating jet. Variation of inlet mass flow rate is considered to analyze the flow characteristics of SJA actuator along with the pressure

Ch-Introduction/images//SJA.png

Figure 1.1: (a) Working principle of Sweeping Jet Actuator [1], (b) Velocity distribution of actuator field [2].

drop, velocity magnitude, formation of vorticity by Kara et al. [11]. Koklu et al. [12] experimentally analyzed how the Coanda extension at exit nozzle can contribute to the actuator's flow control capability in a wind tunnel. The actuation with Coanda extension is applied to Advance Pressure Gradient (APG) ramp model [13] and performance of the actuator on both model is the compared. A parametric extension by Koklu [14] is also conducted on the efficacy to control flow separation with SJA actuator where geometric constraints are explained elaborately. Recent article of Aram et al. [15] explained the interaction of SJA with attached turbulent cross flow using improved delayed detached-eddy simulation(DDES) model. Bohan et al. [16] performed a detailed analysis on oscillation frequency and jet spread angle variation caused by the oscillator scale and working fluid. Cattafesta [17] provided an overview of actuators including classification as well as the working principle of this transducer through controlling the electric signals to avoid disturbance and improving control mechanism. An experimental investigation is performed using an optimized schlieren (two telescope instead of expensive lenses, mirrors or other optical devices. Schlieren is combined with high speed camera to visualize and investigate the internal dynamics of SJA actuator using Fourier transformation, phase information and Hilbert transformation [18]. Ott et al.[19] tried to find out the time-space interface of SJA



actuators for high sweeping frequencies. Another approach on design optimization of SJA actuator to increase peak jet velocity output and pressure drop reduction is carried out by Jeong [20]. An experimental research on Boeing 757 vertical tail [21] that contains 37 SJA actuators was tested under nominal airspeed (100 knots) and found out the best possible situation using 12 SJA actuators, resulting in a significant increase in suction pressure and side force. Park [22] experimentally investigated the thermal properties (convective heat transfer-Nusselt number) and flow distribution of a sweeping jet impingement on a flat wall. Pack [23] experimented in a subsonic channel and found out that active flow controlled high lift system can reduce the excessive drag force and vehicle weight thereby saving the fuel cost. Experimental analysis by Ostermann et al. [24] explained the time-resolved flow field created by fluidic actuator on spatially oscillating jet changing different parameters like velocity ratio, installation angle and Strouhal number. Another experimental analysis [25] is carried out by Park et al. to investigate the effect of internal geometric parameters of oscillators on sweeping jet oscillation distribution.

Ostermann et al. [26] investigated the properties of an oscillating jet in the light of a quiescent environment. A 3D experimental time-resolved approach using a particle image velocimetry (PIV) system to measure velocity field is employed to analyze the property of a sweeping jet emitted from a fluidic oscillator (SJA). For visualization of velocity and pressure distribution Lagrangian and Eulerian techniques are used. The result shows that at the maximum deflection of jet develops stable and periodic repetitive circular vortices. Ostermann et al. [27] experimentally investigated the sweeping jet behavior in crossflow where turbulent mixing occurs. An open return wind tunnel with plates parallel to the oscillating jet flow is used as a setup in a quiescent environment. Velocity field and two stable alternative streamwise counter-rotating vortices are created when oscillating jet exposed to crossflow.

There are other studies on suppressing flow separation of high-speed water and its

associated air bubbles created by the flow using Sweeping Jet Actuator [28]. As it is a multi-phase turbulent flow problem, along with continuity and Navier-Stokes equations, the Eulerian two-phase model was required for the phase-averaged flow field, and the standard  $k-\varepsilon$  model was applied for turbulent simulation. Oscillation frequency, pressure drop at the different mass flow rate, phase angle and jet velocity are the variables needed to be solved for the desired outcome [26]. The cavitation caused due to the oscillating jet was analyzed and improvement of drag force at various flap angles was observed [29].

A recent work [30] on SJA actuator is focused on design modification of SJA to improve flow control performance. A combination of amplifier and actuator is used in active flow control of precessing vortex core (PVC) in a swirl stabilized combustor and at the state of lock-in, distinct PVC and detuning resonance were.

Ahmadabadi [31] proposed a new type of geometry for the fluidic oscillator (consists of a primary and secondary chamber-gradually distributes the jet symmetry) and compared the performance including oscillating frequency and velocity distribution analyzing URANS equation using a 2D-model. The proposed new oscillator has a higher oscillating frequency, lower pressure drop, and a higher output momentum flux compared to the curved oscillator . Alikahassi [32] employed fluidic oscillator to convert the kinetic energy of fluid into the strain energy of the piezoelectric structure through experimental analysis. The position of the piezoelectric beam (where the piezoelectric patch is attached) affects the voltage and power maximization at the natural frequency synchronized with oscillator frequency. Claus et al. [33] finds the relation between internal geometry and external walls by comparing the performance of fluidic oscillator (oscillating frequency) at a different mass flow rate of  $CO_2$ . This also includes geometric modification by varying aspect ratio of exit throat to power nozzle. Coanda effects intensifies three times with increasing the oscillation angle compared to wall effects. Dauengauer et al. [34] analyzed strongly unsteady turbu-

lent jet generation of a fluidic oscillator using Large Eddy Simulation (LES) at various Reynolds numbers (Re). The jet oscillation frequencies from numerical simulation are in close agreement with the experimental measurement. Hossain et al. [35] compared numerical simulation of SJA with experimental results of film effectiveness, thermal field, convective heat transfer coefficient, discharge coefficient at various freestream turbulence levels, and blowing ratios (coolant mass flux to mainstream mass flux). Wen et al. [36] analyzed the effect of internal geometry on its performance. Internal geometry includes the width of the inlet wedge, mixing chamber, exit throat to inlet throat. Obtained results show the effect of inlet wedge at a higher wedge to throat ratio (up to 2) but in the case of a lower ratio (around 0.8), only a stable external sweeping jet is observed without any feedback flow. A small mixing chamber can produce stable sweeping jet motion with a small spreading angle. In the case of exit throat, a larger exit throat can produce stable sweeping motion reducing the blocking effect at the exit. Using 3D LES and experimental visualization drive mechanism of main jet deflection of the angled fluidic oscillator is analyzed in terms of vortex cores, pressure at various mass flow rates [37]. The prime factors for driving the main jet include vortex cores within the mixing chamber, the pressure difference between the feedback channels. Combination of two SJA in back-to-back arrangement sharing feedback channel creates a synchronized sweeping at the exit jet. Based on LES, hot wire and microphone measurements it is observed that acoustic sources generated by the synchronized pressure oscillation of the exiting jet along with large flow length scale near-field direction. Another investigation based on design (using multiple control ports at exit throat) to obtain control over sweep and inclination angle irrespective of supply flow rate. With the help of hot wire, measurement, water flow analysis, numerical analysis, fluidic oscillation is characterized [38]. Oscillation frequency has an inversely proportional relationship with control flow rate up to 5% and 7.7% due to the variation of sweep angle and inclination angle respectively. Similar

work is found with parallel arrangement of fluidic oscillator pair [39]. Tomac et al. [40] introduced another modification in the mixing chamber which enables adjustable frequency at a constant flow rate up to a certain flow rate. The internal flow field was manipulated by fluid injection from the islands of the oscillator into the mixing chamber. Recently, Tajik et al. [41] experimented on the feedback channel and mixing chamber geometry and discovered a polynomial Coanda surface ( $S_2$ ) has positive impact on the velocity profile at the outlet, contributing to significant momentum distribution. Kim et al. [42] numerically investigated the flow physics of suction and oscillatory actuator of compressible turbulent jet using Large Eddy Simulation (LES). Zheng [43] numerically investigated the characteristics of oscillatory frequency of SJA in a quiescent environment with a crossflow of air and found an excellent agreement in terms of the oscillatory frequency and flow field including recirculation bubble with experimental analysis.

These experimental and computational modeling uses wall-mounted hump model,

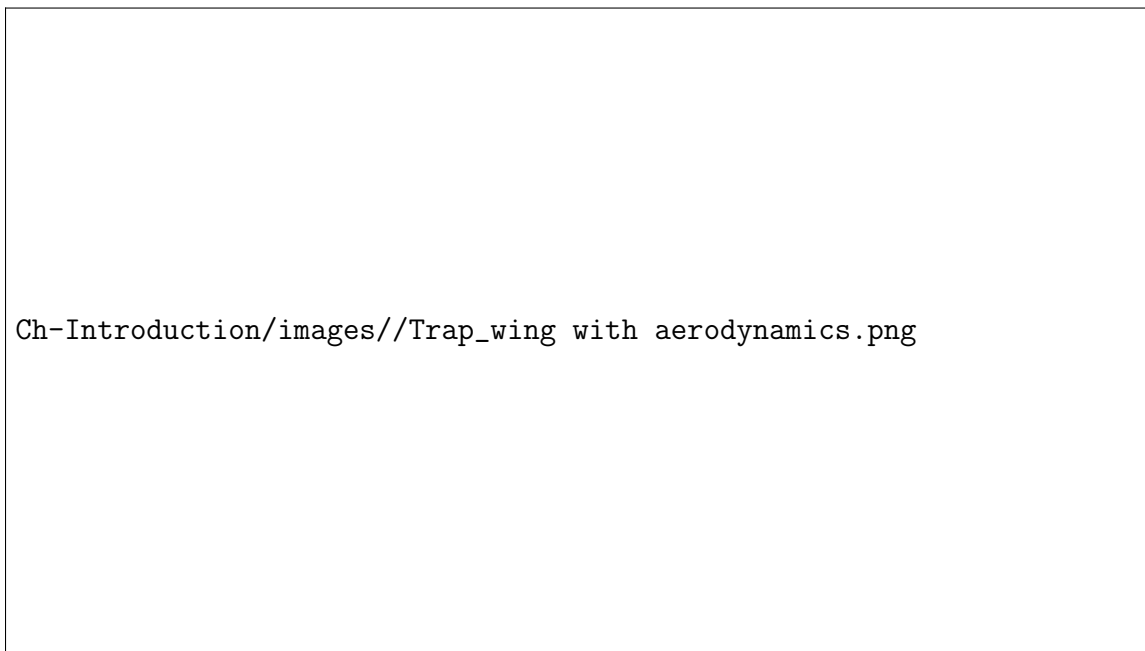


Figure 1.2: Sweeping Jet Actuators integrated at the leading edge of NASA Trap Wing for flow control [3]. (Part of this image is adapted from [4])

canonical hump model, APG ramp model and so on. For example, “NASA Trap

Wing” model has been widely used for CFD simulation benchmarking: to understand the high-speed flow behavior over a swept wing due to its geometric simplicity and ability to capture the complex flow pattern, including flow separation, vortex-shedding, and concurrent boundary layer flow. The configuration has flap, slat, and the main wing in close proximity causing laminar to turbulent flow transition and this creates a challenging case for CFD meshing and computation [44]. McGinley et al. [45] experimented with the high lift configuration to characterize the boundary flow over the wing. To control and observe the flow condition hot-film sensors are installed in the setup and based on sensor data to determine the flow transition and location of the laminar, turbulent regime. Based on strong experimental results numerical models are built. A successful CFD validated model can predict the complex aerodynamics of aircraft accurately enough to reduce the number of expensive experiment conduction and can act as a vital design and optimization tool for improving high-speed commercial systems [46]. Zaman et al. [47] explored the effects of wingtip geometry on wingtip vortices. It was found that the primary descriptor for wingtip vortices is the streamwise vorticity, although mean velocity or turbulence intensity can identify its location and shape. Results showed that the vortex was laminar up to an angle of attack of around  $16^\circ$ , after which it transitions to turbulent. As the angle of attack increases, peak vorticity reaches a maximum at an angle of attack of  $10^\circ$  and remains constant until  $16^\circ$ , after which it begins transitioning. This transition is accompanied by a sharp increase in the turbulence intensity within the core of the vortex, yet there is a sharp decrease in both core peak vorticity and axial velocity. The velocity deficit in the vortex appears to originate from the wake of the airfoil, a portion of which is trapped within the core of the vortex. A numerical investigation is performed on NASA Trap wing geometry obtained from the High-Lift configuration Workshop-I using Star CCM+ [48]. The viscous model chosen for this study is SST  $k-\omega$  and for the laminar, to turbulent flow transition  $\gamma-Re_\theta$  model is used since the

boundary condition has a Mac number of 0.2 there is a laminar to turbulent flow transition occurring in the flow field. Lift and Drag force coefficient and moment coefficient is obtained for different angle of attack and the results are closely aligned with the experimental outcome. Finally, spanwise flow distribution is obtained as a function of pressure coefficient,  $C_p$  at four different locations defined in terms of chord length for 3 different angles ( $13^\circ$ ,  $28^\circ$ ,  $34^\circ$ ) since there is a huge flow separation occurring at a higher angle of attack.

Ives et al.[49] utilized ANSYS Fluent to analyze flow around a NACA 2412 wing. For low speeds and angle of attack less than  $16^\circ$ , turbulence models compared well but still fell below experimental data, the discrepancies increasing with a rising angle of attack. It was found that k- $\epsilon$  was best for airfoil simulation while RSM was best for turbulent wing simulation. Results from the generated model show that freestream velocity has no significant effect on the lift and drag coefficients of the wing. The airfoil, however, experienced a significant change in lift coefficient and a decrease in drag coefficient from high velocity (272.1 m/s) to low velocity (20.73 m/s). This difference in airfoil coefficients is attributed to the appearance of flow separation at a lower angle of attack for lower velocities in comparison to higher velocities. Lower static pressure distribution near the tip of the wing confirmed three-dimensional flow. Holman et al. [50] using XFlow as a tool for analysis of Trap Wings were proven reliable when compared with experimental data. Additionally, the efficiency of its lattice-Boltzmann kinetic particle-based solver was proven. The use of XFlow allowed the presence of moving objects within the simulation and its particle system was able to automatically adapt domain topology to both moving parts and large gradients. A proof-of-concept simulation was conducted of the flap and slat moving from un-stowed to stowed positions. Using a coarse resolution, the code presents an accurate estimation of the linear portions of the lift and drag curves. Using alternative methods for estimating the polar curve, electing to sweep a range of angles, the polar sweep

simulation results were satisfactory.

Over time, focuses are shifting towards higher spatio-temporal precise advancement with simplified physics. Complex non-linear flow can be captured using simple mode decomposing technique from the spectral analysis of the Koopman operator to model a linearize system without losing significant accuracy. Rowley et. al. [51] further presented the “Arnoldi algorithm” that can effectively compute the dominant modes based on snapshots with a successful example in jet crossflow prediction. Schmid et. al. [52] further took Dynamic Mode Decomposition (DMD) by successfully analyzing time-resolved parameters from actual PIV (Particle Image Velocimetry) data and image-based flow distribution of an asymmetric jet. Later on, the application was extended in computational snapshot along with PIV measurements to capture the coherence structure and understand the fluid-dynamical and transport process in plane channel flow, two-dimensional (2-D) cavity, wake flow at the downstream of flexible membrane, and jet passing between two cylinders-creating vortices [53]. Previously, Yamaleev et al. [54] introduced a one dimensional (1-D) time-resolved quasi Euler model to reconstruct the exterior flow characteristics of a three dimensional (3-D) synthetic jet. However, this low fidelity model comes with the limitation in predicting the multidimensional behavior near the jet exit. To address the infinite-dimensional system, Jovanovic et al. [55] introduced a spatially improved DMD algorithm with linear regression data processing. Later on Gomez et al. [56] extended the application for evaluating pressure modes and combined with Karman Filter (KF) to reconstruct the pressure field across the NACA 0012 airfoil. Recursive DMD can identify system frequency better with the combination of POD and DMD-determines the time dynamics through indexing the initial, maximum and final fluctuation stage [57]. Wu et al. [58] showed that reduced order modelling requires noise-free data to work on for reconstruction and prediction of nonlinear systems using channel cross flow. To serve the purpose of improving DMD mode selection, various data pre-processing methods

(i.e. randomized [59], sparsity promoting [55] and compressed sensing [60]).

Throughout the dissertation, we demonstrated various integration conditions and

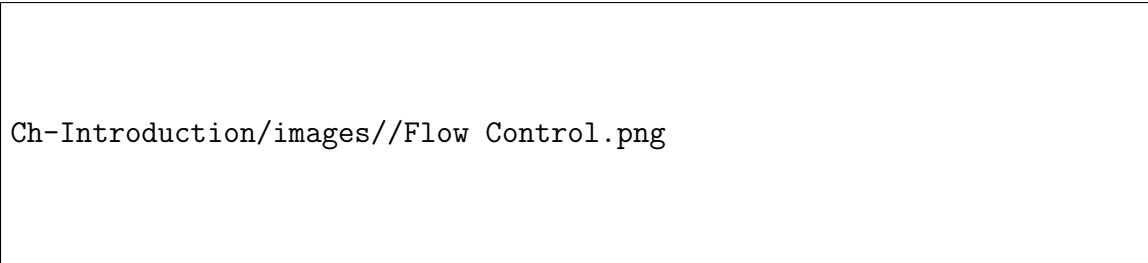


Figure 1.3: Flow control with sweeping jet actuator in NASA hump model[5].

possibilities of SJA. Initially numerical analysis the effect of exit nozzle geometry of SJA in quiescent environment to exhibit the installation flexibility of SJA in a large scale model (i.e. Trap Wing model [3], NASA hump model [5]) is performed. Based on validated CFD model data, ROM is developed based on DMD algorithm to resolve the multiscale issue resulting from multiple SJA along the large scale model. At the same time, ES-DMD elevates the burden of model discretization and computationally expensive iterative solution of full-order model.



Figure 1.4: Geometric variation analysis on exit nozzle of sweeping jet actuator for flexible integration [6].



## CHAPTER II

### The Influence of Exit Nozzle Geometry on Sweeping Jet Actuator

The content of this chapter is published in *Fluids* journal. <sup>1</sup>

#### 2.1 Overview

The SJA increases the local flow momentum without moving parts and is a promising way to suppress aerodynamic flow separation. However, in practical applications, the integration of SJA with curved aerodynamic surfaces results in different exit nozzle geometries from an isolated SJA. This chapter will discuss the effects of exit nozzle geometry on flow physics in a quiet environment. The geometric parameters that we considered are nozzle angle, length, asymmetry, and curvature. A set of time-dependent flow fields are obtained using unsteady Reynolds Averaged Navier-Stokes simulations. Time history of velocity and pressure is recorded inside the SJA feedback channels and downstream of the SJA outlet. The jet oscillation frequency is obtained by employing fast Fourier transform (FFT) for all data sets and compared against the baseline numerical and experimental results. We show that the geometric variations of nozzle exit have a negligible impact on the oscillation frequency. However, there are notable effects on the oscillation amplitude and flow direction, indicating sensitivity to the variation of the exit nozzle.

---

<sup>1</sup>*Alam, M. Kara, K.* (2022). The Influence of Exit Nozzle Geometry on Sweeping Jet Actuator Performance. *Fluids*, vol. 7, no. 2, p. 69.

## 2.2 Introduction

The fluidic oscillator has been studied experimentally earlier to understand the model better, as well as contribute to developing the numerical setup. Cattafesta [17] provided an overview of actuators including classification, as well as the working principle of this transducer through controlling the electric signals to avoid disturbance and improving the control mechanism. The preliminary design of a fluidic oscillator contains two different inlets through which fluids enter into the mixing chamber to create the oscillating frequency. This type of oscillator is termed the “feedback-free oscillator”, and Tomac et al. worked on observing the performance of the fluidic oscillator due to dimensional variation to check the optimal operating range [8]. The result showed a fluctuating behavior of the oscillator with the change of the aspect ratio, size, and fluid type. The extension of this work experimented with the performance of the fluidic oscillator at a lower flow rate (below 3.4 mL/s) [9]. The result showed that both of the jets bifurcated each other without completely cutting off. Raghu et al. [1] focused on different methods to produce sweeping jets along with frequencies and flow rates starting from the history. The fluidic oscillator with feedback channels with a single inlet and two different outlets for producing a pulsing jet was also discussed, which is known as the “angled oscillator”. In Kara et al. [5], a numerical model was developed for analyzing the efficiency of SJA to control the flow separation through active flow control. A two-dimensional (2D) unsteady Reynold’s-averaged Navier–Stokes (URANS) model was used in a wall-mounted hump model with the actuator integrated in an inclined direction. Moreover, the computational fluid dynamics (CFD) simulation extended the future possibility of the three-dimensional (3D) analysis of the hump model. Another article [2] by Kara et al. based on the 3D model of URANS analyzed the internal and external flow over a variety of mass flow rates and determined the pressure drop and the effect on the jet oscillation. The computational analysis was validated with several experimental and numerically proven data

by varying the geometry, type and the working fluid accordingly. A computational study for the characterization of the jet oscillation of the actuator was conducted by Furkan et al. [10] by varying the mass flow rate from incompressible to subsonic compressible flow. This 3D URANS model with a stable mesh structure was proven to be a cost-effective alternative for SJA performance analysis. A notable finding was the constant Strouhal number (implying a stable oscillating flow mechanism) for the oscillating jet. Variation of the inlet mass flow rate was considered to analyze the flow characteristics of the SJA along with the pressure drop, velocity magnitude, and the formation of vorticity by Kara et al. [11]. Koklu et al. [12] experimentally analyzed how the Coanda extension at the exit nozzle can contribute to the actuator’s flow control capability in a wind tunnel. The actuation with the Coanda extension was then applied to the advance pressure gradient (APG) ramp model, and the performances of the actuator on both models were then compared. A parametric extension by Koklu [?] was also conducted on the efficacy of controlling the flow separation with the SJA where geometric constraints were elaborately explained. A recent article by Aram et al. [15] explained the interaction of the SJA with attached turbulent cross-flow using an improved delayed detached-eddy simulation (DDES) model. Bohan et al. [16] performed an excellent analysis of the oscillation frequency and oscillatory spread angle variation caused by the oscillator scale and working fluid.

An experimental investigation was performed using an optimized schlieren. It was combined with a high-speed camera to visualize and investigate the internal dynamics of the SJA using the Fourier transformation, phase information, and the Hilbert transformation [18]. Ott et al. tried to find the time–space interface of SJAs for high sweeping frequencies [19]. Another approach to the design optimization of the SJA to increase the peak jet velocity output and pressure drop reduction was carried out by Jeong [20]. The Boeing 757 vertical tail [21], which contains 37 SJAs, was tested under nominal airspeed (100 kn), and the best possible situation using 12 SJAs was found,

under the no-slip condition through a significant increase in the suction pressure and side force. Park experimentally investigated the thermal properties (Convective heat transfer-Nusselt Number) and flow distribution of sweeping jet impingement on a flat wall [22]. Park experimented in a subsonic channel and found that an AFC-controlled high-lift system can reduce the excessive drag force and vehicle weight, thereby saving on the fuel cost [23]. Experimental analysis by Ostermann et al. [24] explained the time-resolved flow field created by a fluidic actuator on a spatially oscillating jet by changing different parameters such as the velocity ratio, installation angle, and Strouhal number. Another experimental analysis [25] was carried out by Park et al. to investigate the effect of the internal geometric parameters of the oscillators on the sweeping jet oscillation distribution.

The present study is a discussion on the geometric variation of the exit nozzle to understand the flexibility of its installation in a complex system. Moreover, this analysis gives a direction for improving the actuator design effectively in the future.

### 2.3 Numerical Setup and Geometric Details

The baseline geometry considered for the present study was a curved SJA having two feedback channels, a mixing chamber, and an exit nozzle [5, 2, 10, 11]. The baseline CAD geometry can be shared upon request. The actuator performance was studied in a quiescent environment with an extended parabolic flow domain downstream of the exit nozzle (Figure 2.1). The actuator nozzle throat height was  $h = 6.35$  mm. We studied four different shapes of the exit nozzle, namely angle, L-top, L-both, and curvature (Figure 2.2). For our angle case, we changed the exit nozzle angle from  $70^\circ$  to  $130^\circ$  with an increment of  $10^\circ$  gradually to observe the frequency and variation in the flow distribution. For the curvature case, it was the nozzle length. We varied the exit nozzle length from  $0.70 h$  to  $1.30 h$  with  $0.10 h$  increments and correspondingly changed the curvature radius. We created the arc by keeping the

tangent with the base (nozzle length) and normal. Similarly, nozzle length variation was adopted with 0.10 h increments (for our baseline case, the nozzle length was 0.86 h) for the L-top and L-both cases. The only difference was in L-top: the top arm length was adjusted based on the nozzle length, and the other arm was kept constant as the baseline (0.86 h); for the L-both case, both nozzle arms were varied.



Figure 2.1: Computational domain of the SJA and the flow field (baseline).

## 2.4 Governing Equations

The present study required a time-based solver model for a single-inlet mass flow (as mass flux) for which unsteady Reynold's-averaged Navier–Stokes (URANS) equations for mass continuity, momentum, and energy conservation were considered [2] and the



Figure 2.2: Schematic diagram of the sweeping jet actuator including the tested geometric parameters of the exit nozzle, **(a)** angle, where  $\theta$  = half exit nozzle angle, **(b)** top arm length variation, L-top, **(c)** both arm lengths' variation, L-both, and **(d)** curvature, where L = nozzle length.

shear stress transport (SST)  $k-\omega$  model was chosen for turbulence closure. We studied a single mass flux ( $J = 66.12 \text{ kg/m}^2\text{s}$ ) (inlet mach number,  $M_i = 0.16 < 0.3$ ) at the subsonic level, but fully turbulent compressible flow was considered since the variation of the Mach number exceeded 0.3 at the exit nozzle throat (maximum Mach number,  $M_{max} = 0.627 > 0.3$ ) [61–63].

The governing equations are given below:

Continuity equation:

$$\frac{\partial \bar{\rho}}{\partial t} + \frac{\partial(\bar{\rho} \bar{u}_i)}{\partial x_i} = 0 \quad (2.1)$$

Here,  $x_i$  are the spatial coordinates and  $u_i$  is the velocity components, and since it is an unsteady analysis ( $\bar{\rho}$ ), density is a function of time.

Momentum equation:

$$\frac{\partial(\bar{\rho} \bar{u}_i)}{\partial t} + \frac{\partial(\overline{\rho u_i u_j})}{\partial x_j} = -\frac{\partial \bar{P}}{\partial x_i} + \frac{\partial[2\bar{\nu}_T \bar{S}_{ij} - \overline{\rho u_i'' u_j''}]}{\partial x_j} \quad (2.2)$$

Here,  $\nu_T$  is the kinematic eddy viscosity and  $S_{ij}$  the mean strain-rate tensor, and pressure  $\bar{P}$  was obtained from the ideal gas law. Energy equation:

$$\begin{aligned} \frac{\partial}{\partial t} \left[ \rho \left( \bar{e} + \frac{\bar{u}_i \bar{u}_i}{2} \right) + \frac{(\bar{\rho} \bar{u}_i'' \bar{u}_i'')}{2} \right] + \frac{\partial}{\partial x_j} \left[ \bar{\rho} \bar{u}_j \left( \bar{h} + \frac{\bar{u}_i \bar{u}_i}{2} \right) + \bar{u}_j \frac{\overline{\rho u_i'' u_i''}}{2} \right] = \frac{\partial}{\partial x_j} \left[ -q_{Lj} - \overline{\rho u_j'' h''} + \overline{t_j i u_i''} \right. \\ \left. - \overline{\rho u_j'' \frac{1}{2} u_i'' u_i''} \right] + \frac{\partial}{\partial x_j} \left[ u_i (2\bar{\nu}_T \bar{S}_{ij} - \overline{\rho u_i'' u_j''}) \right] \end{aligned} \quad (2.3)$$

where  $\bar{e}$  is the specific internal energy and  $\bar{h}$  the specific enthalpy, and  $q_L$  was determined using Fourier's law of conduction. The working fluid considered here was air with the consideration of the ideal gas density  $\rho_{in} = 1.183 \text{ kg/s}$ , and the molecular

viscosity was taken based on the three-coefficient method of Sutherland’s law:

$$\mu_T = \mu \frac{T^{3/2}(T_o + S)}{T_o(T + S)} \quad (2.4)$$

[15]where the reference viscosity  $\mu_o = 1.716 \times 10^{-5}$  kg/(ms), reference temperature  $T_{ref} = 273.16$  K, and effective temperature  $S = 110.56$  K, and the reference static pressure was taken as atmospheric pressure (=101,325 Pa).

### 2.4.1 Computational Fluid Dynamics Model

The flow regime was assumed as fully turbulent for which the SST k-w model was chosen among the URANS models along with the continuity, momentum, and energy equation. The coupled scheme with second-order accuracy was used for solving the pressure, momentum, kinetic energy, and dissipation rate. The turbulence effect was combined using the standard two-equation kinetic energy, k, and energy dissipation,  $\omega$ , with the shear stress transport constraint making this model suitable for our study.

The second-order discretization was used for pressure, and the second-order up-wind formulation was used for the density, momentum, turbulent kinetic energy, specific dissipation rate, and energy. For time-accurate simulation, the bounded second-order implicit scheme was adopted. The residual for the transport equations was considered up to  $10^{-6}$ .

## 2.5 Mesh Independence Test

The internal geometry of the sweeping jet actuator has a complex flow physics, and to capture the accurate flow pattern, the flow domain for computation needs to be very precise. To optimize the truncation and round-off error and validate the discretized domain for unsteady simulation, a mesh independence test was required. For the present study, four different (2D) surface meshes were produced considering



the exit nozzle height ( $h = 6.35$  mm) as a critical parameter. CFD fluent meshing was performed using ANSYS-2020. The mesh names were based on the element size, which was a function of the characteristic length,  $h$ . SST  $k-\omega$  was used for turbulent closure. Wall  $Y^+$  was kept less than one to resolve the actuator boundary. Ten layers were used near the actuator wall with the first layer thickness  $h/500 = 0.0127$  mm. The details of the tested mesh can be found in Table 2.1. The final mesh chosen for simulation was N-60, which contained 396,973 quadrilateral and 369 triangular elements with a maximum skewness of 0.71889. Therefore, N-60 indicates that the number of elements along the exit nozzle is 60 and the element size is  $h/60$ . Similarly, N-40, N-50, and N-80 have element sizes of  $h/40$ ,  $h/50$ , and  $h/80$ , respectively. For a gradual increment of the element size, two spheres of influence were used having radii of  $7.5 h$  and  $20 h$  with a growth rate of 1.15 [10, 2]. The mesh name was based on the element size chosen for the smaller sphere, but for the entire structure, the element size was controlled by keeping a tenth of the characteristic length (N-10) (Figure 2.3), except for N-80, which was considered to be exact, so we used an element size of N-40 for the entire flow domain. Figure 2.4 shows the sampling data at three different loca-

Table 2.1: Mesh details for computation.

Mesh Name	Total Number of Elements	Total Number of Nodes
N-40	199,489	201,155
N-50	288,969	290,932
N-60	397,342	399,634
N-80	1,008,947	1,012,880

tions for 0.02 s. Based on the pressure signals, fast Fourier transform (FFT) analysis was conducted, which converts the signal into the frequency domain and captures the peak to determine the oscillation frequency of the system. The computational setup was stabilized using 10,000 time steps with a step size of  $1 \times 10^{-5}$  s, and after that, data sampling analysis was performed on bi-stable oscillation for 0.1 s with the same step size. A pressure-based solver setup was used with a velocity inlet of 55.8 m/s, which corresponds to a mass flow rate of 6.8 g/s, and the ambient pressure outlet

condition was considered. Eventually, further analysis on the diffuser was performed using the same mass flow rate. The mesh independence test was performed on the baseline geometry [5].

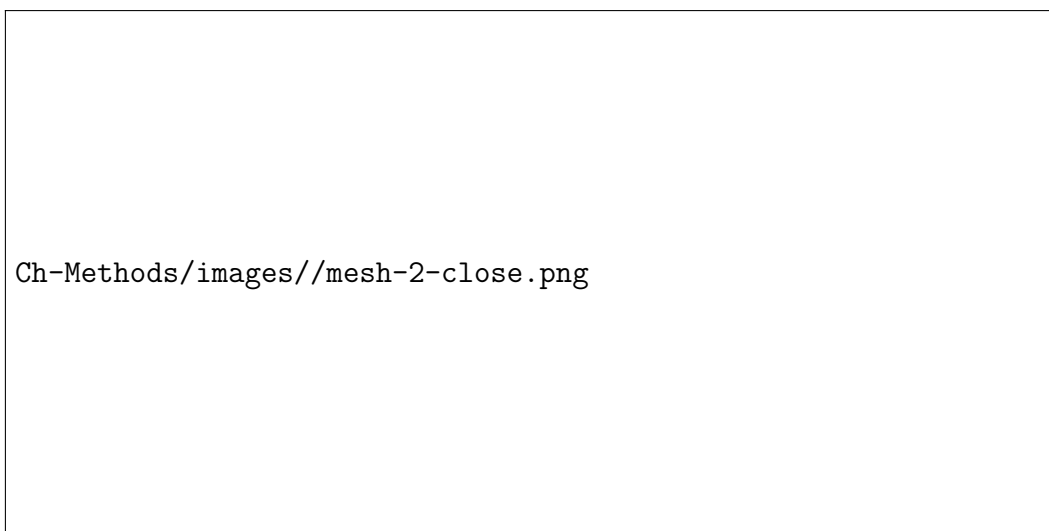


Figure 2.3: **(Left)** SJA geometry showing the position of different sampling points,  $uf$ ,  $lf$ , and  $x6y0$ , exit nozzle height,  $h$ , exit nozzle length,  $l$  and (red circle) used for focused meshing. **(Right)** Close view of the mesh near the exit nozzle.

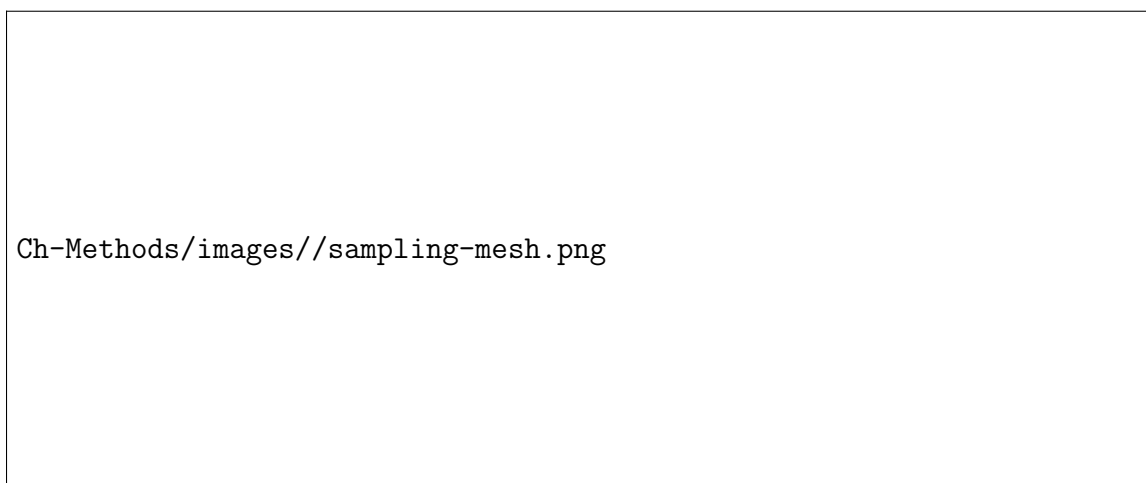


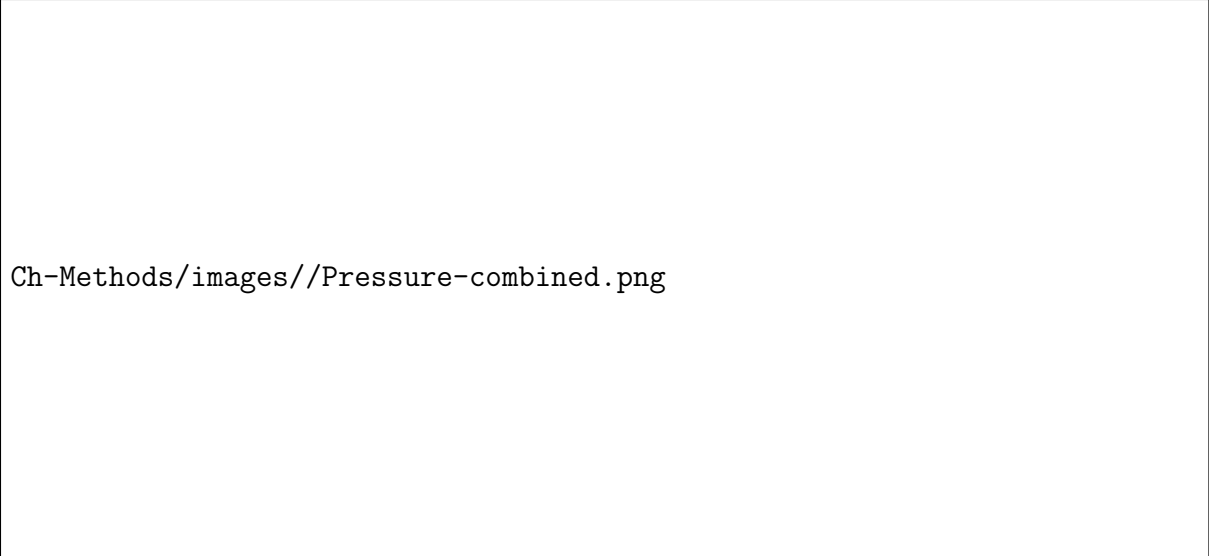
Figure 2.4: **(a)** Time history at (P- $uf$ ), (P- $lf$ ), and (P- $x6y0$ ) showing the pressure amplitude for N-60 and corresponding FFT analysis **(b)** at those sampling locations where peaks indicate the oscillation frequency.

FFT analysis results showed that the oscillation frequency from mesh N-60 was stable for the actuator. Pressure sampling can provide better signals for the power spectral density (Figure 2.5). In addition, time-averaged analysis was performed on

the mean pressure and velocity along the centerline for the various mesh setups and using MATLAB; local error analysis was conducted using cubic spline interpolation on N-80 to match the number of data points for each mesh setup. From Figures 2.6 and 2.7, we can observe that the N-60 mesh distribution was quite reasonable to capture the flow distribution (the maximum error was 5.5%). Therefore, based on both the time-averaged and unsteady results, N-60 was chosen for further analysis.

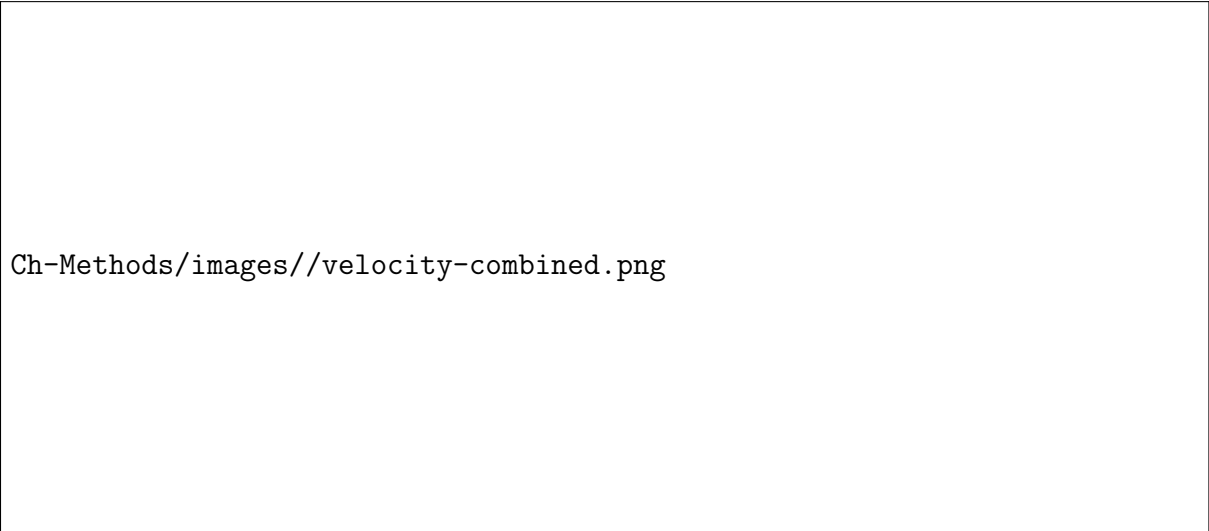


Figure 2.5: Oscillation frequency obtained from FFT analysis for 0.1s at different sampling points based on the velocity magnitude ( $v$ ) and static pressure ( $p$ ): downstream,  $x6y0$  (6 mm, 0 mm), upper feedback channel,  $uf$  (-25.4 mm, 19 mm), and lower feedback channel,  $lf$  (-25.4 mm, -19 mm), for different mesh distributions.



Ch-Methods/images//Pressure-combined.png

Figure 2.6: Local error analysis of the mean pressure along the centerline based on the finest (N-80) mesh. The mean pressure is normalized by the inlet  $P_{in} = 128,961.46$  Pa.



Ch-Methods/images//velocity-combined.png

Figure 2.7: Local error analysis of the mean velocity along the centerline based on the finest (N-80) mesh. The mean velocity is normalized by the inlet mean velocity  $V_{in} = 44.83$  m/s.

## 2.6 Model Validation and Verification

The present study was based on a single mass flow rate ( $=6.8$  g/s) in terms of the mass flux as the inlet condition, and we compared both the numerical and experimental data including the oscillatory frequency and Strouhal number for the corresponding

mass flow rate. As our data included both validation and verification for our case, they gave a strong foundation to our model for the further case study. Table 2.2 shows that the 2D numerical model can determine the oscillatory frequency quite well compared to the 3D model in terms of error % obtained from the experimental result [64]. The Strouhal number also showed a very good agreement with the 3D simulation [10].

Table 2.2: Model validation and verification.

<b>Ref.</b>	<b>Analysis Type</b>	<b>Strouhal Number</b>	<b>Oscillation Frequency</b>	<b>Error</b>
Slupski [64]	Experimental	0.0160	337.70 Hz	-
Furkan [10]	Numerical (3D–URANS)	0.0131	341.80 Hz	1.21%
Present Study	Numerical (2D–URANS)	0.0134	350.04 Hz	3.64%

## 2.7 Results and Discussion

The sweeping jet actuator is an active flow control device having a diffuser, mixing chamber, and feedback channel, and it produces a bi-stable spanwise oscillation at the downstream exit nozzle. The computational setup for this study was similar to the mesh independence test. The geometric modifications were based on the critical dimension; the exit nozzle throat and the variation of the parameters were analyzed after that location. Based on the mean velocity ratio ( $\eta\% = V_{case}/V_{Baseline} * 100$ ) obtained at a downstream ( $x/h = 5$ ) location, we evaluated the efficiency of the respective geometry [10, 65]. The red color in the error bars indicates an efficiency lower than the baseline, where the blue bars are the baseline and the green bars show an efficiency higher than the baseline case. The FFT was performed at the upper and lower feedback channel since these locations were consistent for all the geometries. Table 2.3 manifests the oscillation frequency for each case based on pressure sampling. The mean pressure and velocity distribution at the centerline were obtained from the time average of instantaneous velocity and pressure for 0.1 s. The half-jet width was

measured at the  $x/h = 5$  location for all the cases. It was defined as the distance between two points where the peak means the velocity drops by half. The half-jet width indicates the jet spreading downstream influenced by the exit nozzle [65]. Since the curvature cases showed the most promising results, instantaneous total pressure at the centerline was studied to analyze the pressure drop downstream.

Table 2.3: Oscillation frequency for different cases at the upper and lower feedback channel.

Curvature								
Sampling Points	0.86h*	0.70h	0.80h	0.90h	1.00h	1.10h	1.20h	1.30h
P-lf(Hz)	350.04	348.03	349.84	349.96	349.97	360.91	360.03	360.98
P-uf(Hz)	350.01	349.16	350.09	349.91	349.96	360.03	360.96	360.10
Angle								
Sampling Points	35deg	40deg	45 deg	50deg*	55deg	60deg	65deg	
P-lf(Hz)	359.03	359.03	359.84	350.04	350.05	339.98	339.98	
P-uf(Hz)	359.96	359.54	359.93	350.01	350.28	340.23	340.10	
L-top								
Sampling Points	0.86h*	0.70h	0.80h	0.90h	1.10h	1.20h	1.30h	1.50h
P-lf(Hz)	350.04	339.98	350.16	350.03	350.24	349.91	350.03	350.43
P-uf(Hz)	350.01	340.10	350.13	350.40	350.03	349.90	350.17	349.96
L-both								
Sampling Points	0.70h	0.80h	0.86h*	1.10h	1.20h	1.30h		
P-lf(Hz)	340.11	340.91	350.04	349.97	350.03	359.84		
P-uf(Hz)	339.91	339.98	350.01	350.42	350.17	359.16		

\* Baseline; P-lf, pressure sampling data at the lower feedback channel; P-uf, pressure sampling data at the upper feedback channel.

### 2.7.1 Effect of Curvature

The nozzle exit length varied from 0.70 h to 1.30 h with 0.10 h increments, and the curvature radius changed accordingly. Compared to the straight nozzle exit (baseline), the curved nozzle exit caused higher dispersion in the velocity (Figure 2.8a). Because of the Coanda effect, the jet tended to adhere to the curved nozzle exit surface, causing the uniform distribution of velocity at the exit nozzle. Compared to the baseline case where the higher velocity was observed after the exit nozzle and then suddenly dropped from  $x/h = 5$ , the curvature resulted in a higher mean velocity

downstream. The velocity ratio at point  $x/h = 5$  showed that the efficiency could be increased as much as 51.98% (0.80 h) compared to the baseline case. The instantaneous velocity contour plot for the extreme cases (0.70 h and 1.30 h) can be found in the Supplementary Material. As expected, Figure 2.11b depicts the gradual reduction of the pressure at the downstream exit nozzle for the curvature cases, following the same pattern as the velocity. In addition, the instantaneous pressure showed an overall pressure drop at the downstream location, influenced by the curvature radius (Figure 2.10). Finally Figure 2.8a shows that the oscillation downstream was uniform and symmetric for all the cases along with the baseline. In the FFT analysis (Table 2.3), the magnitude of the oscillation frequency varied within 10.94 Hz compared to the baseline case. However, it followed a trend with the shortest length (0.70 h) having a lower frequency (348.03 Hz) and the maximum length (1.30 h) having the highest frequency (360.98 Hz), while the frequency changed as much as 10 Hz between 1.00 h and 1.10 h.

Ch-Methods/images//Curvature-velocity.png

(a) Curvature Case

Ch-Methods/images//angle-velocity.png

(b) Angle Case



Ch-Methods/images//L-both-velocity.png

(c) L-both Case

Ch-Methods/images//L-top-velocity.png

(d) L-top Case

Figure 2.8: **(I)** Mean velocity along the centerline normalized by the inlet velocity,  $V_{in,Baseline}$ ; **(II)** velocity ratio,  $\eta$  at point  $x/h = 5$ .

### 2.7.2 Effect of Exit Nozzle Angle

To understand the angle effect, the nozzle exit angle was varied from  $30^\circ$  above and  $30^\circ$  below the baseline case. Figure 2.8b shows the time-averaged velocity magnitude along the centerline of the SJA at different nozzle exit angles. As expected, before the exit nozzle throat, the velocity distribution was almost constant for all the cases. The peak velocity was observed right after the exit nozzle throat, and downstream, the mean velocity dropped for all the cases, except  $45^\circ$ , compared to the baseline case. The velocity ratio at point  $x/h = 5$  showed that only for the  $45^\circ$  case, we obtained an efficiency at the  $x/h = 5$  location higher than the baseline case (2.34%). The minimum efficiency at that point was 39.15% at  $40^\circ$ . A similar trend can be seen in the pressure field (Figure 2.11a) as well. The mean pressure distribution along the centerline for the angle cases showed a slight variation in the local pressure. For the smallest angle ( $\theta = 35^\circ$ ), we obtained the maximum pressure downstream (after  $x/h = 5$ ). Therefore, the angle cases showed the erratic behavior of the velocity and pressure in the symmetry axis.

FFT analysis exhibited that the oscillation frequency varied from 340Hz to 360Hz, within 3% of the frequency of the baseline actuator (Table 2.3).

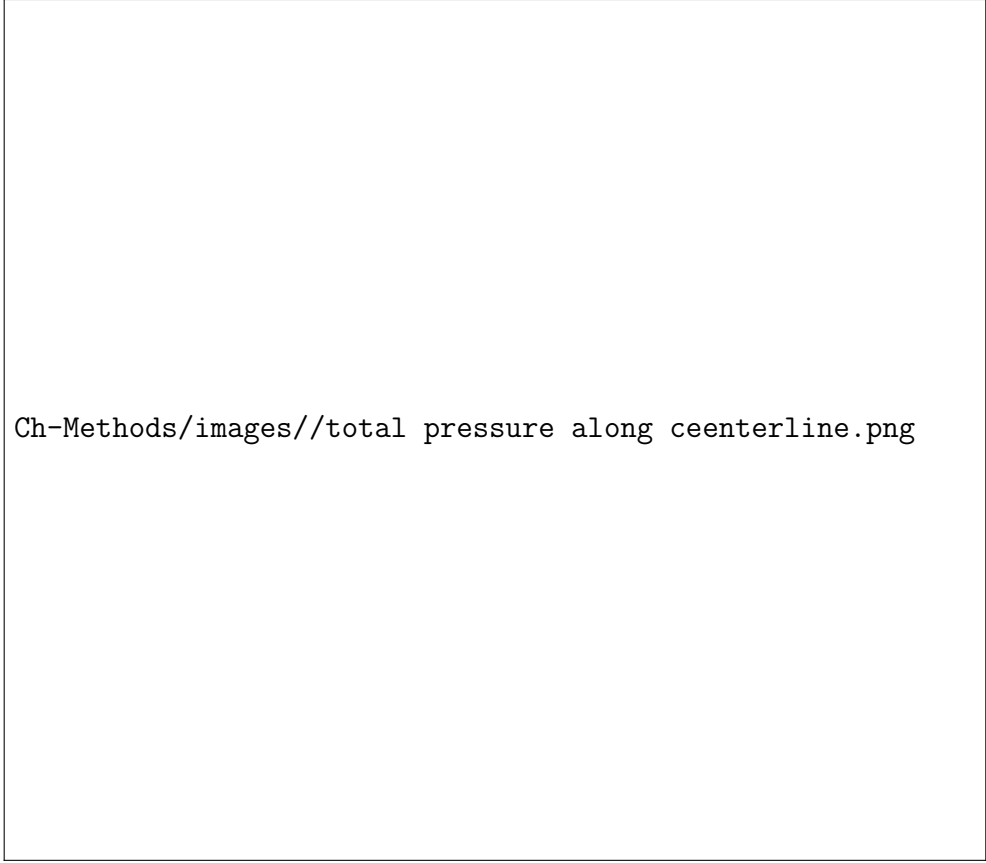
### 2.7.3 Effect of Length: Both Nozzle Arms

We studied the L-both case by adjusting the exit nozzle length from 0.70 h to 1.30 h, which increased the nozzle length gradually (both nozzle arms), keeping the baseline case (0.86 h) in between. This resulted in the velocity dropping off 20 m/s after the exit nozzle, which made the shorter nozzle arm length convenient for applications (Figure 2.8c). From the velocity ratio at  $x/h = 5$ , it was evident that the velocity decreased gradually starting from 0.70 h to 1.30 h, and the lowest efficiency was 37.37% for the longest arm length (1.30 h) compared to the baseline. The results showed that the increment of the nozzle length caused a slight average pressure rise

(Figure 2.11c). From the FFT analysis (Table 2.3), it was observed that there was no significant variation in the oscillation frequency (3% with respect to the baseline).



Figure 2.9: At  $x/h = 5$ , **(a)** half-jet width for curvature, L-top and L-both cases (in terms of nozzle length,  $x/h$ ) and angle case (in terms of the half-exit angle,  $\theta$ ). **(b)** Velocity profile for the curvature case.



Ch-Methods/images//total pressure along ceenterline.png

Figure 2.10: Instantaneous total pressure along the centerline normalized with the total inlet pressure,  $P_{total,Baseline} = 131,829.66$  Pa for curvature cases.

Ch-Methods/images//angle and curvature-pressure.png

Ch-Methods/images//L-top and L-both-pressure.png

Figure 2.11: Mean pressure along the centerline normalized by inlet,  $P_{in,Baseline}$  for (a) Angle, (b) Curvature, (c) L-both and (d) L-top.

#### 2.7.4 Effect of Length: Top Nozzle Arm (Asymmetry)

The variation on one side (top) of the exit nozzle length was studied where the other arm of the exit nozzle was kept the same as the baseline for the convenience of the comparison. As the analysis extended from 0.70 h to 1.50 h (the baseline arm length was 0.86 h), this study could reasonably predict the variation for the bottom length

cases as well. Compared to the baseline case geometry, the velocity (Figure 2.8d[a] ) for  $L_{top}$  decreased with the gradual increment of the arm’s length downstream of the exit nozzle, which indicates asymmetric flow distribution downstream (the velocity profile is given in the Supplementary Material). When focused at  $x/h = 5$ , it was observed that (Figure 2.8d[b]) the 0.70 h, 0.80 h, and 0.90 h cases performed slightly better compared to the baseline. The velocity ratio decreased up to 52.88% for the longest arm length studied. In the case of pressure (Figure 2.11d), the longest length had the most gradual increment along the symmetry axis downstream of the diffuser. The oscillation frequency here had a similar magnitude as the baseline (Table 2.3). For all the studied cases (Figure 2.9a), the half-jet width is plotted against the respective parameters (half-exit angle, nozzle length) to compare the jet spreading with the baseline case. From the angle case, a  $40^\circ$  half-exit angle provided the maximum spreading (0.07252 m higher than the baseline) downstream because of the dual peaks of the mean velocity. In the curvature case, there was a trend showing that the spread gradually decreased from 0.70 h to 1.30 h. For the L-top cases, the jet width increased up to 0.90 h, and then it went down as the nozzle length increased. Finally, L-both showed an upward trend with the nozzle length: higher nozzle length kept the fluid flow attached to the sidewalls, therefore contributing to jet spreading.

## 2.8 Discussion

The present study investigated the effects of exit nozzle geometry on the performance of the sweeping jet actuator (SJA). First, we validated the discretization of the baseline case and obtained a close agreement with the previous experimental and numerical studies by performing a detailed mesh independence test. In the time-accurate analysis, we used compressible 2D URANS model with the SST  $k-\omega$  turbulent closure, which is computationally inexpensive, yet reliable compared to other full order model (i.e.LES). Then, four different geometric parameters are employed at the exit nozzle

region since this is the most crucial part emitting the oscillating jet.

Systematic length adjustments is performed to understand the effect on the oscillation frequency in detail and external flow fields- the mean flow velocity and pressure distribution of the SJA. To obtain the oscillation frequency of the studied system, we performed FFT analysis on four discrete sampling points at critical locations. We found that pressure signals can provide more consistent data than velocity signals. We provided further evidence by performing the FFT analysis on each signals. This analysis further showed that the oscillation frequency is not dependent on the external geometry rather it is a function of the internal shape variation as observed in a previous study [41]. However, for the curvature case, the mean velocity at the downstream of the exit nozzle was 51.98% higher than the baseline at  $x/h = 5$ . This validated the effect of shapes can enhance coanda effect which eventually results in increased jet spread after the exit nozzle. Among the studied shapes L-top, L-both, and curvature, each 0.10 h increment in the arm's length caused a reduction of 9% in the average velocity downstream. Here, the L-top cases created asymmetry in the oscillating jet, and the flow tended to adhere to the longer arm sidewalls. The angle variations showed an erratic behavior for the flow distribution. Low angle width causes congestion at the diffuser exit affecting jet spreading and gradual stretching angle shows the initial dominance of adhesion, coanda effect and later flow detachment from the diffuser arms. We observed a negligible mean pressure variation between the cases studied. In conclusion, the SJA design needs to be modified with the curved exit nozzle configuration for better flow control and uniform jet spreading performance.

## CHAPTER III

### Analysis of High-Frequency Jet Oscillation using Dynamic Mode Decomposition with Eigenvalue-Based Selection Algorithm

This chapter is adopted from *Analysis of High-Frequency Jet Oscillation using Dynamic Mode Decomposition with Improved Eigenvalue-Based Mode Selection Algorithm*, Physics of Fluids (under review).<sup>2</sup>

#### 3.1 Overview

When pressurized with a fluid, a sweeping jet actuator (SJA) emits a self-induced and self-sustained continuous but spatially oscillating jet at the outlet. The SJA increases the local flow momentum without moving parts and is a promising way to suppress aerodynamic flow separation. The dynamic mode decomposition (DMD) algorithm captures the oscillating behavior of complex non-linear flow structures by identifying the low-rank coherent structures and superimposing the dominant modes to reconstruct the system. The basis vectors (modes) are determined using the Koopman theory. They are applied to develop an accurate shallow rank structure from a non-linear complex sweeping jet actuator flow field in the present study. With spectral decomposition, DMD can identify the dominant patterns in the oscillating flow structure - making it a valuable tool for spatio-temporal data extraction. Since the algorithm has no hyper-parameter, it is flexible to implement in any periodic flow distribution to determine the temporal behavior. We have modified the classical DMD

---

<sup>2</sup>*Alam, M., Kara, K. (2022), Analysis of High-Frequency Jet Oscillation using Dynamic Mode Decomposition with Improved Eigenvalue-Based Mode Selection Algorithm. Physics of Fluids (under review)*



algorithm using amplitude-based data filtration for better accuracy and flexibility on computationally obtained raw data. For analysis, we considered velocity and pressure data series of a sample window around the exit nozzle in a 2D sweeping jet actuator flow field for time step sensitivity and dominant mode requirement for reconstructing and predicting the coherent structure for various mass flow rates.

### 3.2 Introduction

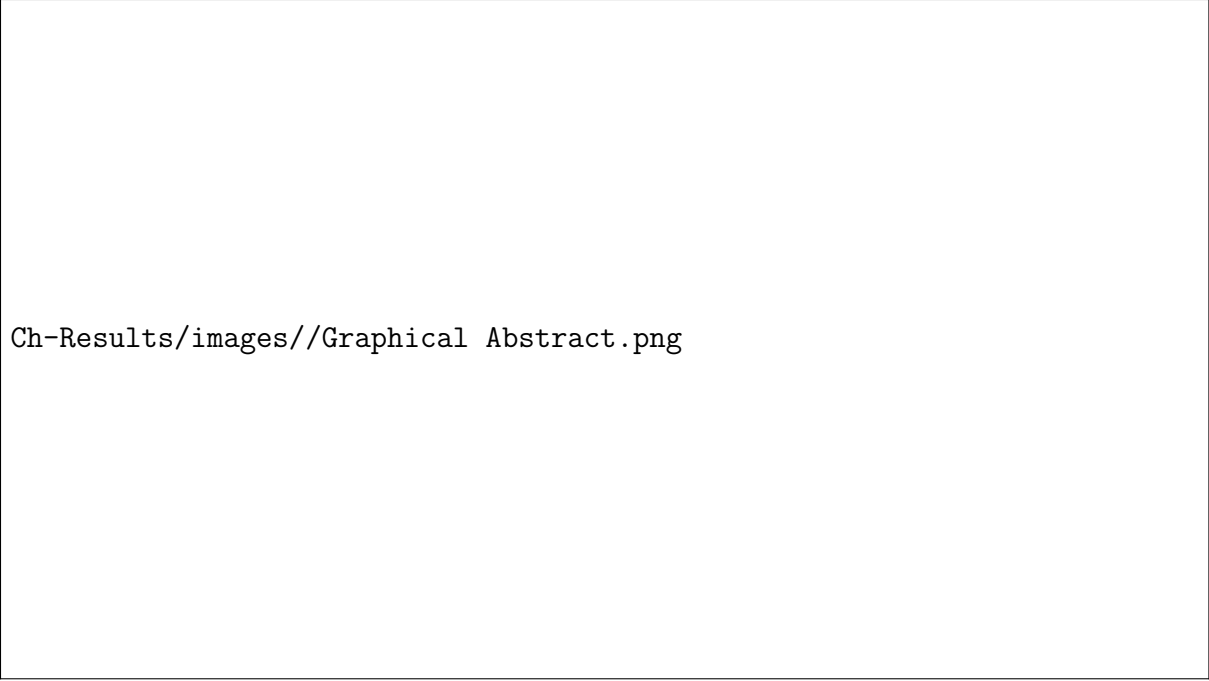
Large-scale aircraft modeling puts constrain on time-step and element size selection for stable dynamic simulation. It becomes computationally challenging to adjust the selection of domain setup with the integration of small-scale devices like SJA to analyze the flow control performance. CFD can provide a very reliable but high-ranked practical flow field by solving complex nonlinear governing equations iteratively. To elevate the computational expense, focuses are shifting towards higher spatio-temporal precise advancement with the help of reduced order modeling (ROM). Complex nonlinear flow can be captured by identifying the coherent pattern using a simple mode decomposing technique from the spectral analysis of the Koopman operator to model a linearized system without losing significant accuracy. Rowley et al.[51] presented the Arnoldi algorithm that can effectively compute the dominant modes based on snapshots with a successful example in jet crossflow prediction. Schmid et. al.[52] further took DMD by successfully analyzing time-resolved parameters from particle image velocimetry (PIV) data of an image-based flow distribution of an asymmetric jet. Later on, the application was extended in computational snapshot along with PIV measurements to capture the coherent structures and understand the fluid dynamics and transport process in plane channel flow, 2D cavity, wake flow downstream of the flexible membrane, and jet passing between two cylinders-creating vortices[53, 52]. Yamaleev et al.[54] introduced a one-dimensional (1D) time-resolved quasi-Euler model to reconstruct the exterior flow characteristics of a three-dimensional (3D) synthetic

jet. However, this low-fidelity model comes with the limitation in predicting the multidimensional behavior near the jet exit. To address the infinite-dimensional system, Jovanovic et al.[55] introduced a spatially improved DMD algorithm with linear regression data processing. Later on, Gomez et al.[56] extended the application for evaluating pressure modes and combined it with Karman Filter to reconstruct the pressure field across the NACA 0012 airfoil. Recursive DMD[57] can identify system frequency better with the combination of proper orthogonal decomposition (POD) and DMD because it determines the time dynamics through indexing the initial, maximum, and final fluctuation stages. Wu et al.[58] showed that ROM requires noise-free data to work on for the reconstruction and prediction of nonlinear systems using channel cross flow. To serve the purpose of improving DMD mode selection, various data pre-processing methods has been introduced (i.e. randomized[59], sparsity promoting[55], compressed sensing[60]).

The DMD is a versatile dimensionality reduction tool using singular value decomposition on a sequential data set. Its application started as a post-processing tool[66]. Classical DMD algorithm performs rank reduction based on POD modes only[67]. This ROM algorithm can easily convert a highly non-linear system into a low-rank linear state by identifying the recurrent pattern of the dynamical system[68]. Over time, various sorting algorithms are introduced like amplitude based[69], bayesian[70] and extended DMD[71].

The sweeping jet actuator has taken special attention for emitting self-sustaining induced jet without any energy consumption. To compute this highly non-linear periodic system, experimental and numerical results are combined with various features such as sparse[55], recursive[57], lagrangian[72] technique to accurately reconstruct and predict the flow distribution using DMD algorithm. The oscillating behavior of the sweeping jet is influenced by the geometry and inlet conditions[11, 2, 10, 73, 41, 74, 75]. Higher frequency can cause asymmetry in the flow field resulting in modeling

difficulty. For this reason, it has been modeled with higher density fluid(i.e. water), and lower inlet mass flow conditions for smooth periodic oscillation suitable for non-intrusive ROM models. Additionally time-delay embedding[76] helps to capture the time dynamics on such stabilized systems at lower oscillation frequency[77, 78]. Time-delay embedding can provide a more temporally accurate result but creating the Hankel matrix (time-delay embedded data) might add up the considerable computational difficulty. To resolve these issues, the present study aims toward an eigenvalue-based DMD algorithm that can work on a high-frequency sweeping jet actuator (SJA) model to capture the spatially nonlinear and complex time dynamical oscillating system. Application for active flow control includes bigger domain such as wing configuration[79–81], hump model[5, 82] and practical simulation includes 3D configuration to resolve. Evidently, unsteady simulation for these larger configurations is computationally expensive and reasonable to use macro flows (larger  $\Delta t$ ). But due to its smaller size, multiple actuators are required to be integrated to observe the flow control effect. This causes two difficulties: finer mesh requirement at the actuator regions which increases the number of elements exponentially to discretize the integrated domain and smaller timestep adjustment i.e.micro flows are needed near the actuator domain ( $\Delta t < 10^{-4}$ s)[64]- causing the simulation prohibitively expensive[83, 84]. To address this problem, we proposed an improved DMD algorithm focusing on periodic oscillation patterns for high-frequency systems (Fig. 3.1). This Efficient DMD algorithm can be implemented for high-frequency periodic oscillation instead of using constant velocity [85] to capture the real flow quantity with reasonable accuracy and apply as boundary condition without discretizing and simulating those small flow control devices in the model. The present analysis exhibits successful implementation of the oscillating pattern of velocity and total pressure using reduced order modeling. This can radically improve the simulation scenario of big domain geometry with integrated small volume elements in a time-dependent environment.



Ch-Results/images//Graphical Abstract.png

Figure 3.1: Outline for the dimensionally-reduced spatio-temporal system analysis using sorted DMD algorithm and its application.

The present study aims for accurate reconstruction of flow parameters of three different high-frequency Sweeping Jet Actuators using a modified DMD algorithm for various time steps. The flow parameters include the velocity and pressure flow field and profile. To achieve higher accuracy eigen value-based sorting and time-embedding[76] are convoluted in the standard DMD algorithm. Proposed algorithm can facilitate simplified SJA model to integrate in complex system (i.e. High Lift Wing configuration[86, 3], Ahmed body[87, 88]) to understand flow topology accurately yet in a computationally efficient manner.

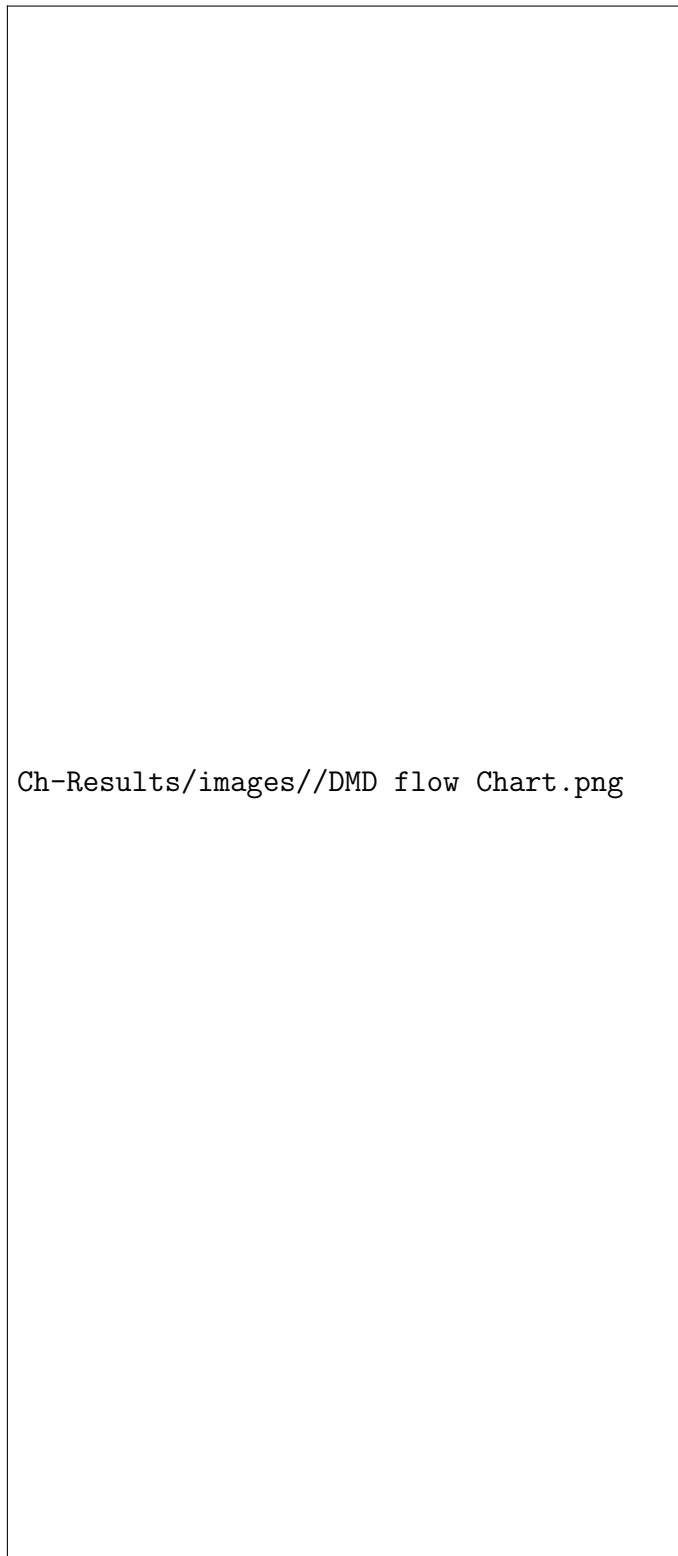
### 3.3 Methodology

The standard DMD algorithm truncates the later modes from Singular value decomposition (SVD) based on the hierarchically arranged singular values (Fig. 3.2). The dominant modes contain the spatial information of the flow field, the real part of the eigenvalues indicates the growth and decay rates and the imaginary part includes

the oscillation frequency of the corresponding modes[76]. But this method is insufficient with higher rank truncation for complex nonlinear systems because it could not preserve the discrete frequency with the modes.[89] In addition to truncating the negligible singular value (close to zero) from the SVD decomposition, we tested a couple of amplitude-based selection criteria for DMD truncation and introduced an eigenvalue-based sorting to improve the algorithm without the cost of time-delay embedding[58]. Later on, for profile reconstruction and prediction we compensated the insufficient spatial information effectively using time-delay embedding[78] along with the eigenvalue-based truncation. The model includes singular value decomposition to capture the dominant modes with considerable information, time-embedding, and sorting of the modes based on eigenvalues, then truncation of the rank of the matrix to build the ROM model for reconstruction and future prediction. Previous studies are based on a low-frequency system where the spatial modes require higher attention than the time dynamics. We introduced a weight function based on Koopman modes to quantify rank truncation and demonstrated its capability to select the dominant modes to gain stability and accuracy in the flow field. Then we compared our proposed algorithm with the best sorting method from the state of art. The compatibility of these models is tested with high spatially and temporally resolved CFD sample data. The algorithm detail is discussed in the outline section (Alg. 1).

### **3.3.1 DMD Outline**

It was first applied to the fluid dynamical system by Schmidt[55], later on, time-delay embedding is introduced[78] which offered a major advantage of providing further spatial information: additional information improves the Koopman operator to reconstruct the time-dynamics of the system. The drawback of time-delay embedding is it makes the data matrix prohibitively larger for the highly nonlinear system: increasing the computational expense. For our high-frequency system, we implemented the



Ch-Results/images//DMD flow Chart.png

Figure 3.2: DMD Flow Chart

DMD algorithm by modifying the time coefficient based on eigenvalues and performed further rank truncation instead of time-delay embedding[69]. This eigenvalue-based sorting can preserve the time dynamics better which works quite accurately on the high-frequency oscillating system without further computational cost. Later on, for sparse profile data (1D) we applied time-delay embedding which provides the desired boundary condition of the actuator model.

For our system let,  $X$  be the high rank data (x-velocity, pressure) matrix ( $n \times m, n > m \in \mathbb{R}$ ) and it is resolved into two matrices ( $X_1$  and  $X_2$ ) such that  $X_1 = [x^1, x^2, \dots, x^{m-1}]$  and  $X_2 = [x^2, x^3, \dots, x^m]$  collected up to  $m$  range of time,  $t = [t^1, t^2, \dots, t^m]$  where the time steps,  $\Delta t$  are:  $1 \times 10^{-5}, 2 \times 10^{-5}, 5 \times 10^{-5} s$ . Each tall skinny  $x$  vector represents the entire high-rank spatial information (2D flow field,  $n=90821$  and 1D flow profile,  $n=263$ ) of each snapshot.

$$X = \begin{bmatrix} | & | & & | \\ x^1 & x^2 & \dots & x^m \\ | & | & & | \end{bmatrix}, \quad x^1 = \begin{bmatrix} u_1 \\ u_2 \\ \cdot \\ \cdot \\ u_n \end{bmatrix} \quad (3.1)$$

For profile development, 1D (line) data is used that created an under-determined system ( $n=263$ ). To resolve this problem, time-delay embedding is convoluted along with the sorting criteria. The new data matrix is taken into Hankel space as follows:

$$H^1 = \begin{bmatrix} u_1 & u_2 & \dots & \dots & \dots \\ u_2 & u_3 & \dots & \dots & \dots \\ \dots & \dots & \dots & \dots & \dots \\ \dots & \dots & \dots & \dots & \dots \\ u_l & u_{l+1} & \dots & \dots & u_n \end{bmatrix}, \quad H^2 = \begin{bmatrix} u_2 & u_3 & \dots & \dots & \dots \\ u_3 & u_4 & \dots & \dots & \dots \\ \dots & \dots & \dots & \dots & \dots \\ \dots & \dots & \dots & \dots & \dots \\ u_l & u_{l+1} & \dots & \dots & u_n \end{bmatrix} \quad (3.2)$$

Here,  $l$  is the number of time-delay embedding. Now the system becomes,

$$H^2 \approx \hat{A}H^1, \quad (3.3)$$

similar to the original data matrix but with a higher rank structure. In the present study, we focused on the stable pressure and velocity data of the actuator flow field. DMD aims to obtain the best fit linear operator  $A$  for a given nonlinear periodic system such that:

$$\frac{dx}{dt} \approx Ax. \quad (3.4)$$

The numerically obtained result is arranged as time-based snapshots and the number of periodical waves optimal for a given system is studied based on the presented algorithm. DMD identifies the leading eigenvalues and eigenvectors by performing SVD on the data matrix: three components are obtained  $U$ ,  $\sigma$  and  $V^T$  where  $U$  and  $V$  are orthonormal matrices containing the spatial and temporal information respectively and  $\sigma$  is the diagonal matrix which contains the singular values (energy of each mode) hierarchically. The highest energy content is the zero frequency mode which is the mean velocity of the flow field[58]. DMD algorithm reduces the rank of the system based on those singular values by truncating the negligible elements. But unlike POD modes energy is more distributed in DMD modes and each DMD mode contains a distinct frequency[90].

$$SVD[X] = U\sigma V^T \quad (3.5)$$



where reduced version becomes,

$$\sigma = \begin{bmatrix} \sigma_1 & \dots & \dots & \dots \\ \dots & \sigma_2 & \dots & \dots \\ \dots & \dots & \dots & \dots \\ \dots & \dots & \dots & \sigma_m \end{bmatrix} \approx \begin{bmatrix} \sigma_1 & \dots & \dots \\ \dots & \dots & \dots \\ \dots & \dots & \sigma_r \end{bmatrix} = \hat{\sigma}, \quad (3.6)$$

$$U_{n \times n} \approx \hat{U}_{r \times r}, \quad V^T_{m \times m} \approx \hat{V}^T_{r \times r} \quad (3.7)$$

after truncation the rank becomes  $r$  where,  $r < m \in \mathbb{R}$ , consequently  $U$  and  $V^T$  reduces into  $r$  by  $r$  matrices. Now, instead of the original high-ranked approximation, we obtain the reduced model  $\hat{A}$  from the moore-penrose pseudo inverse of  $\hat{U}$  and  $\hat{V}^T$  (Eq. 3.9).

$$X^2 \approx \hat{A}X^1 \quad (3.8)$$

where,

$$\hat{A} = \hat{U}^T \hat{\sigma} \hat{V} X^2 \quad (3.9)$$

Best fit for  $\hat{A}$  for rank  $r$  can be obtained in Frobenius norm where the error is minimized using least square optimization Eq. 3.10,

$$\arg \min \|X^2 - \hat{A}X^1\|_F = \hat{U} \hat{\sigma} \hat{V}^T, \|\hat{A}\|_F = \sqrt{\sum_{i,j} (\hat{A}_{ij})^2} \quad (3.10)$$

Solving  $\hat{A}$  for eigen decomposition we obtain  $\lambda$  and  $\omega$ ,  $\Phi$  contains the spatial information (Eq. 3.11) of the DMD modes and  $\lambda$  contains the temporal correlation in the reduced domain,

$$\hat{A} = \omega \Lambda \omega^{-1} \quad \text{modes}, \Phi = \hat{U} \omega \quad (3.11)$$

After SVD-based rank truncation, we obtain a square matrix suitable for eigen decomposition. DMD modes can be extracted by indexing the amplitude,  $b$ [69](Fig. 3.3). For our case, we sorted the modes based on the magnitude of real eigenvalues. After discretizing by DMD algorithm we can obtain (Eq. 3.12) the continuous time-dynamics from  $\lambda$  and the timestep,  $\Delta t$ :

$$\alpha_i = \frac{\ln \lambda_j}{\Delta t}, \quad \text{where, } \lambda_j = \text{diag}(\Lambda) \quad (3.12)$$

Finally, for reconstruction and prediction in the original high rank space, a linear function is used (Eq. 3.13):

$$X_{new}^n = \sum_{j=1}^r b_j \Phi_j^n e^{\alpha_j t_j}, \quad b_j = \Phi_j^{-1} u_2 \quad (3.13)$$

### 3.3.2 Selection of DMD Modes

Amplitude(= $b$ ) is the least-square solution of the observable for the spatially dominant modes. It works as a weight function for selecting modes; we performed an in-depth sensitivity analysis along with the eigenvalue spectrum observations[69, 90]. We have chosen the system frequency of 131.75Hz for detailed analysis to obtain selection criteria. Following is the flow field analysis result for the number of modes=150,  $\Delta t = 5 \times 10^{-5}$  s, number of snapshots used is 360 for three full periods. We took a further one full period for future prediction. Note that 20% of the total modes are required for successful reconstruction, however, 31.25% of total modes are considered for short-time prediction stability. We documented the corresponding percentage to total modes. For total modes  $n$ ,  $r$  are integers,  $n \geq r \in \mathbb{R}$ . Based on weight function  $\kappa$  mode truncation is performed. Weight function,  $\kappa$  can be quantified as:

$$\beta_i = \sqrt{b_i}, \kappa = \frac{\beta_1 + (\beta_1 + \beta_2) + \dots + (\beta_1 + \beta_2 + \dots + \beta_n)}{\sum_{i=1}^n \beta_i} \% \quad (3.14)$$

---

**Algorithm 1** ES-DMD: Eigenvalue Based Sorted Dynamic Mode Decomposition
 

---

1 \* . For 1D data set addition spatial information is embedded in Hankel space (Eq. 3.2, Data Matrix  $X$  becomes Hankel matrix  $H$ ,

$$X^1 \rightarrow H^1, \quad X^2 \rightarrow H^2$$

1. (High Spatial Data: 2D) The matrix  $X$  is resolved into two same size data matrices such that  $X^2$  is one time step ( $\Delta t$ ) advanced than  $X^1$ ,

2. Perform SVD on  $X^1$   $U\sigma V^T = \text{SVD}(X^1)$

3. Rank truncation

$$\hat{U} = U[:, 1:r]$$

$$\hat{V} = V[:, 1:r]$$

$$\hat{\sigma} = \sigma[1:r, 1:r]$$

4. Low-rank dynamics  $\hat{A} = \hat{U}^T \hat{V} \hat{\sigma}^{-1} X^2$

5. Eigen decomposition  $[\omega, \Lambda] = \text{eig}(\hat{A})$

6. Dominant modes  $\Phi = \hat{U}\omega$

7. Dominant mode spectrum (Eigenvectors and values)

$$\lambda_j = \text{diag}(\Lambda), \quad \alpha_j = \frac{\ln(\lambda_j)}{\Delta t}$$

8. Compute amplitude, sort in descending order and choosing modes ( $mr$ )

$$b_j = \Phi_j^{-1} u_2, \quad mr = \text{real}(\lambda), \quad \mathbf{ind} = \text{sort}[:, mr]$$

$$\Phi_{new} = \Phi[:, \mathbf{ind}]$$

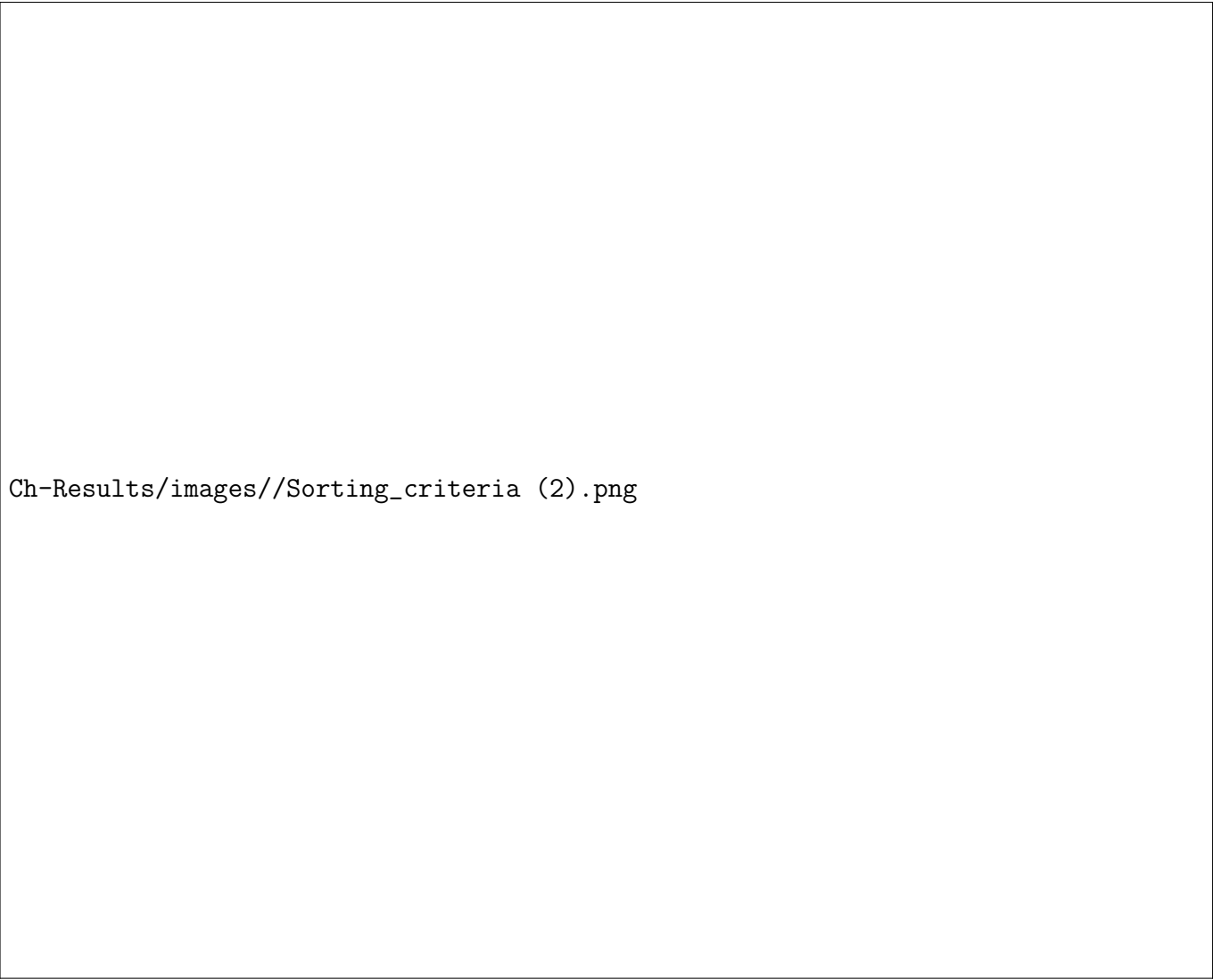
$$\alpha_{new} = \alpha[\mathbf{ind}]$$

$$\mathbf{b}_{new} = \mathbf{b}[\mathbf{ind}]$$

9. Reconstruction and Prediction

$$\mathbf{X}_{new}^n = \mathbf{b}_{newj} \Phi_{newj}^n e^{\alpha_{newj} t_j}$$


---



Ch-Results/images//Sorting\_criteria (2).png

Figure 3.3: Working principle of different DMD sorting criteria based on modes,  $N = 150$  for system frequency,  $f = 131.75\text{Hz}$ .

Fig. 3.3 shows for a fixed number of modes,  $N=150$  the percentage of cumulative relative magnitude with the corresponding reconstruction and accuracy scenario for the system.

### 3.3.2.1 Sorting Criteria-1:Based on Amplitude

We adopted the weight function for rank truncation. The first index,  $I$  is chosen based on the absolute amplitude,  $b$  (Eq. 3.13). Since  $b$  is a complex conjugate, we took the absolute values to arrange the magnitude.

$$I_i = |b_i| \quad (3.15)$$

In Fig. 3.3(a), based on 80% of the cumulative weight function if we choose 31.25% of the total dominant modes we can obtain an absolute error of 12% where, we normalized the flow fields with the corresponding maximum field data and then defined the difference as absolute error:

$$abs(E_i) = \left| \frac{CFD_i}{max(CFD_i)} - \frac{DMD_i}{max(DMD_i)} \right| \quad (3.16)$$

Fig. 3.4 shows the corresponding eigenvalues of the selected modes. The concentrated focus on growth rate is required to capture local bi-stable oscillation of the flow field.

### 3.3.2.2 Sorting Criteria-2:Based on Growth/Decay Rate

Another sorting criteria[69] focusing on the growth and decay rate for DMD modes are used for indexing the modes:

$$I_i = |b_i|(e^{-\sigma_i} + e^{\sigma_i}) \quad (3.17)$$

Here, 150 modes correspond to 63% of the weight function, and following the trend, it can produce the flow field with 52% accuracy. This criterion is similar to the time integrating sorting but here it just focuses on the amplitude, growth, and decay rate, not the temporal advancement. Based on this index the eigenvalues are uniformly distributed within the spectrum. Fig. 3.3(b) shows some regions in the flow domain has out of range values within our label.

### 3.3.2.3 Sorting Criteria-3:Based on Amplitude with Time

Ahmed [91] introduced a sorting criteria evaluation integrating spatial amplitudes with time-averaged growth/decay rates over the time span of the system. The sorting index is as follows,

$$I_i = |b_i| \frac{e^{\sigma_i T} - 1}{\sigma_i T} \quad (3.18)$$

We used the same weight-based selection criteria for truncation and the same number of modes here can occupy 28.47% of the weight function and gives partial reconstruction at the high amplitude regions of the system. Furthermore, eigenvalues(Fig. 3.4) show that since its indexing focuses on decay rates of the system more, excluding some values at the oscillating domain. It basically chooses the modes considering the shallow rank system as a unitary matrix.

### 3.3.2.4 Sorting Criteria-4: Based on Eigenvalues

Based on previous sorting criteria, we studied the corresponding Eigen spectrum and obtained the dominance of the growth rate for our studied data. Therefore, we introduced a sorting criterion where eigenvalues are chosen congregating towards the growth region. The importance index is quantified by the hierarchical arrangement

of real eigenvalues,  $\lambda$ .

$$I_i = \text{real}(\lambda_i) \quad (3.19)$$

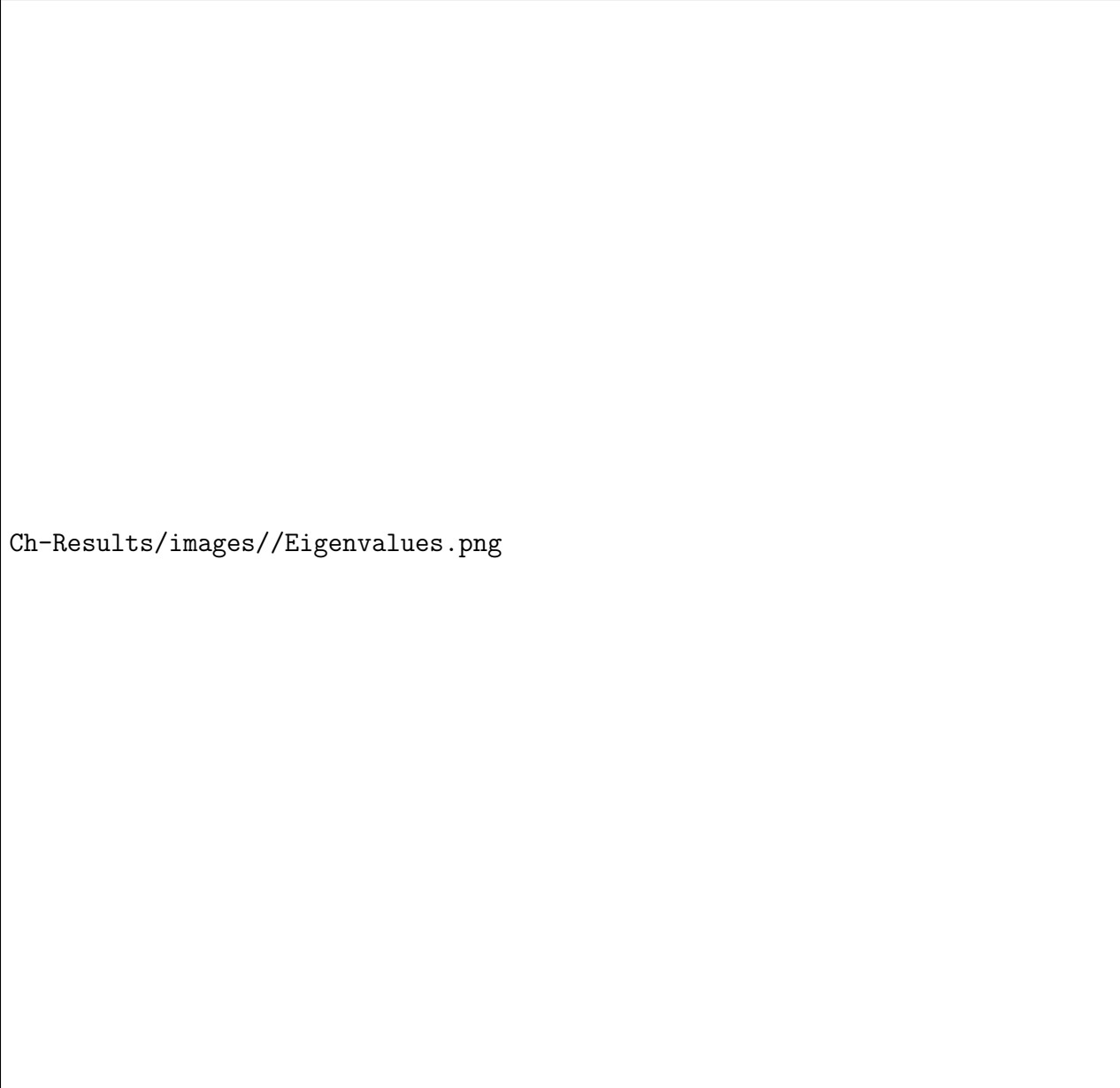
After sorting we obtain the reduced matrix as positive definite (since only the positive eigenvalues are chosen based on magnitude). Since this sorting criterion is not based on amplitude, but  $\lambda$ , we quantified it based on  $\epsilon$  cumulative energy content,  $\epsilon CEC$ :

$$\epsilon CEC = \sum_{k=1}^N \frac{\text{real}(\lambda_k)^2}{\sum_{i=1}^N \text{real}(\lambda_i)^2} \quad (3.20)$$

Furthermore, these criteria can capture perfectly even the local peaks in the oscillating system and we modified the initial amplitude formula to obtain better performance in the future prediction as well by using,

$$b_j = \Phi_j^{-1} u_2, \quad \text{instead of } u_1 \quad (3.21)$$

This small modification gave us better control over prediction without losing accuracy in the reconstruction phase. Note that based on conventional energy content (i.e. singular values) choosing modes might not be always reasonable to capture the important features of a system[92]. This sorting criterion provides a smoother transition and dominant mode number selection compared to the other sorting criteria (Fig. 3.3). For DMD this paper presents a reasonable basis for choosing the number of modes for each system.



Ch-Results/images//Eigenvalues.png

Figure 3.4: Corresponding eigen values of the chosen modes,  $N = 150$  for system frequency,  $f = 131.75\text{Hz}$  and time-step,  $\Delta t = 5 \times 10^{-5}\text{s}$  for four sorting.

For our oscillating system, the positive part of real eigenvalues (non-negative) is more important indicating the accuracy-dependence on capturing the growth rate in the dominant modes (Fig. 3.4). Negative real eigenvalues are responsible for the decay rate of the system and the imaginary part of the eigenvalues provides the oscillation frequency of the corresponding modes, selection criteria provide a vital role in the



accuracy of the model. The present study includes three different time steps for validating the compatibility of the algorithm. The most challenging case-the largest considered time-step (i.e.  $\Delta t = 10^{-4}s$ ) gives the best possible reconstruction for the highest frequency system (i.e.  $250.04Hz$ ) with almost ( $\approx 20\%$ ).

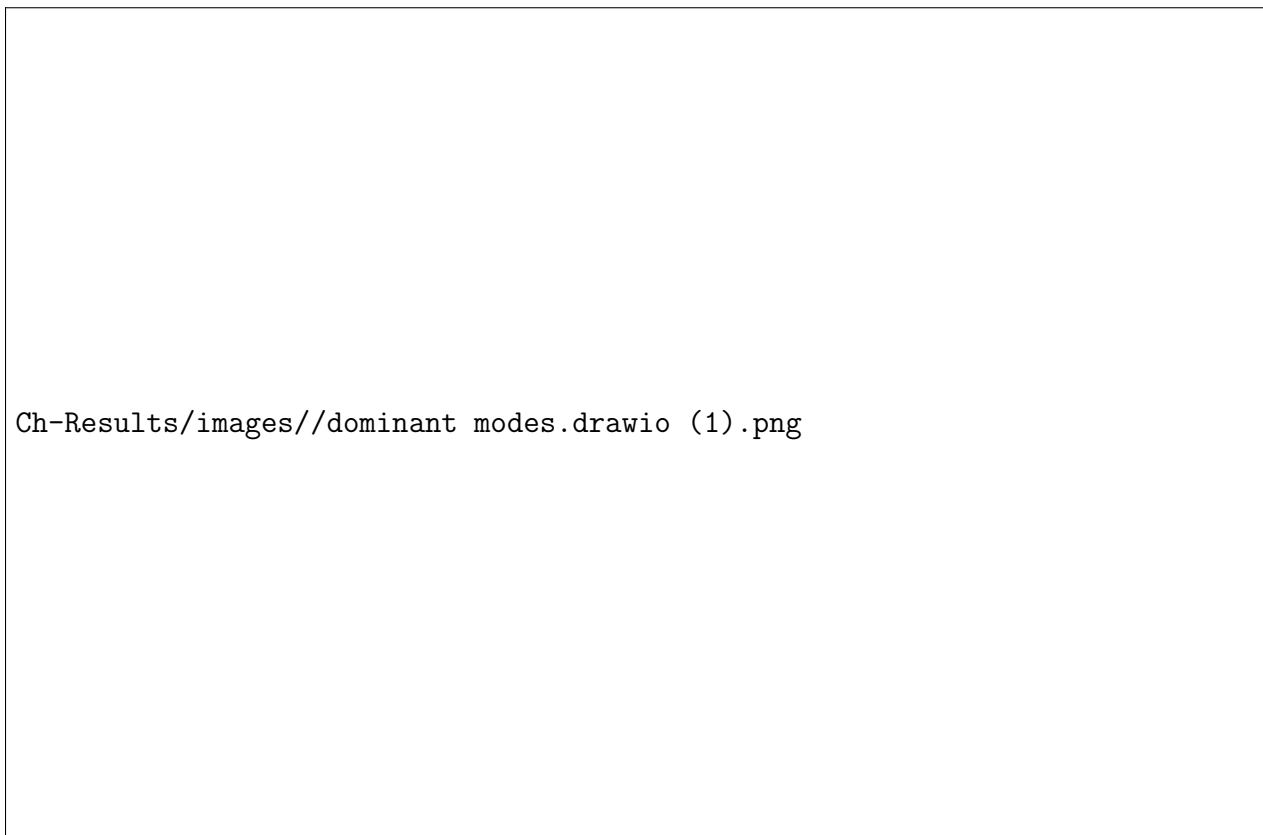


Figure 3.5: First 4 discrete dominant modes of our proposed sorting criteria-4 showing the coherent pattern of the flow.

### 3.3.3 Results

Complex flow distribution of Sweeping Jet Actuator in quiescent environment is studied for three different mass flow rate- 0.0025lb/s, 0.005lb/s, 0.01lb/s. In each case, data is taken for three full periods of snapshots respectively. Observable for the system are u-velocity and total pressure for three different time steps. After performing the DMD algorithm we need to: (1) choose the sorting criteria, (2) select the rank of the system, (3) choose a suitable time step. After investigating several selection

criteria [91] for DMD modes in the most challenging case (Highest frequency, largest time steps) we have used absolute amplitude indexing for our system. Later, we demonstrated the effect of selection criteria can accurately project high rank original space for various time steps ( $\Delta t_1=2 \times 10^{-5}s$ ,  $\Delta t_2=5 \times 10^{-5}s$ ,  $\Delta t_3=10^{-4}s$ ), frequency (Case-I: 85.85Hz, Case-II: 131.75Hz, Case-III: 250.04Hz) and flow parameters (u-velocity and total pressure). Successful implementation of the DMD algorithm requires 99% of total energy utilization [58]. Fig. 3.4 tends to preserve the real positive eigenvalues for DMD modeling of the system. Based on this pattern, we introduced a new sorting criterion that can be used for reconstructing bistable oscillatory systems. Local deviation from the true data is accepted within 12% of the 2D-CFD result for the 2D flow field.

Since our system has large amplitude and gradual growth rate, this sorting criterion along with the first ones are chosen for further analysis based on the absolute error for a given number of modes. We shared a comparative analysis result to validate our algorithm's performance for the chosen system. Fig. 3.5 shows the spatial contribution of the first four discrete dominant modes from sorting criteria-4. (From left) the first mode corresponds to the mean flow of the system, the second mode shows two simultaneous flow of high and low magnitude exerting from the exit nozzle (left boundary in each figure), eventually, the number of flow patterns keep increasing. This shows how frequently each pattern is to be considered in the dominant modes. Dominant modes show the recurring patterns required to grasp the oscillating characteristics across time.[93] However, to compare on the same scale we have used an identical number of modes for each sorting criteria for our system data. Based on this sorting analysis, sorting criteria-1 and 4 can provide 88% of accuracy whereas sorting-2 and 3 can preserve very only 10% and 52% of the true results. So, we choose the two best sorting criteria (Based on accuracy) -sorting-1 and sorting-4 for our further analysis. Fig. 3.4 shows the eigenvalues distribution of the corresponding

modes chosen for DMD construction for different sorting criteria. Here frequency has a proportional relation with the DMD modes. For example, to capture 88% of accuracy we need 20% of the dominant modes (in terms of reconstruction) for mass flow rate = 0.005lb/s which is 4 times higher(=4.80%) than case-I ( $\dot{m}=0.0025\text{lb/s}$ ) and 1.5 times lower(=30.5%) than case-III ( $\dot{m}=0.01\text{lb/s}$ ).



Figure 3.6: Comparison between CFD and DMD result for  $s_1$  at the center point (0,0) data for (a)  $\Delta t = 2 \times 10^{-5}$  s, (b)  $\Delta t = 5 \times 10^{-5}$  s, (c)  $\Delta t = 10^{-4}$  s for system frequency,  $f = 131.75$  Hz and modes,  $N = 150$ .  $u^*$  and  $t^*$  are normalized velocity and time period.



Figure 3.7: Comparison between CFD and DMD result for S4 at the center point (0,0) data for (a)  $\Delta t=2 \times 10^{-5}$ s, (b)  $\Delta t=5 \times 10^{-5}$ s, (c)  $\Delta t=10^{-4}$ s.  $u^*$  and  $t^*$  are normalized velocity and time period.

In this section, we will demonstrate the reconstruction and prediction result of


the chosen criteria for our exit nozzle sampling windows for different oscillation frequencies. The exit nozzle sampling window contains very dense mesh resulting in a large number of elements(=90821) for each snapshot. Therefore, we have chosen two full period data irrespective of the step size for each case and showed the prediction result for the next two periods. For error analysis, we documented the mean square error for the sampling field for each snapshot, and for local analysis, we used point probe sampling performance from both algorithms (Sorting-1 and Sorting-4) for comparison.

### 3.3.3.1 Sensitivity Analysis for Time Step

An optimum time step is essential for analyzing the system. If the time step is infinitesimally small compared to the system it might result in large sets of data analysis for a given period. On top of that, larger snapshot frequency can cause negligible variation in consecutive snapshots-resulting inconsistency between the spatial modes and the time dynamics. For this reason, it is required to optimize the dynamics of each frequency system to perform the time-step sensitivity. We used  $\Delta t_1=2 \times 10^{-5}$ s,  $\Delta t_2=5 \times 10^{-5}$ s,  $\Delta t_3=10^{-4}$ s step size which corresponds to snapshot frequency 50,000Hz, 20,000Hz and 10,000Hz respectively. Fig. 3.6,3.7 shows that for the center line sampling probe (0,0) the u-velocity and total pressure for 4 full periods. The First 3 periods are used for reconstruction and the last one is exhibiting the performance of prediction. We showed two different sorting algorithms for performance analysis. Our proposed algorithm can perfectly capture the periodicity as well at the local peaks for the oscillating point compared to sorting criteria-1. In the prediction part, it also follows the oscillating pattern and the parameters up to 25% of the full period (orange shaded region), Whereas sorting-1 only focuses on the time dynamics but fails to capture the local peaks in reconstruction and gets skewed at the peaks in the prediction phase. Fig. 3.8 refers to the global performance indication for the

algorithms at three different studied time steps. For all the time steps studied the root mean square error is less than 0.07 at the reconstruction phase for both algorithms and in the prediction, it increases expectation-wise since the DMD algorithm is linear and can only be able to capture periodicity for prediction, not the spatial peaks associated with it. This global error analysis shows the stability of the algorithms for the studied time step. For the future study, we would choose the maximum possible time-step which is  $\Delta t=10^{-4}$ s for computational efficiency. Equation for root mean square error (RMSE) for each snapshot is given below:

$$RMSE = \sqrt{\frac{\sum_{j=1}^N (Y_{CFD,j} - Y_{DMD,j})^2}{N}} \quad (3.22)$$



RMSE\_timestep\_m005\_flowdomain.png

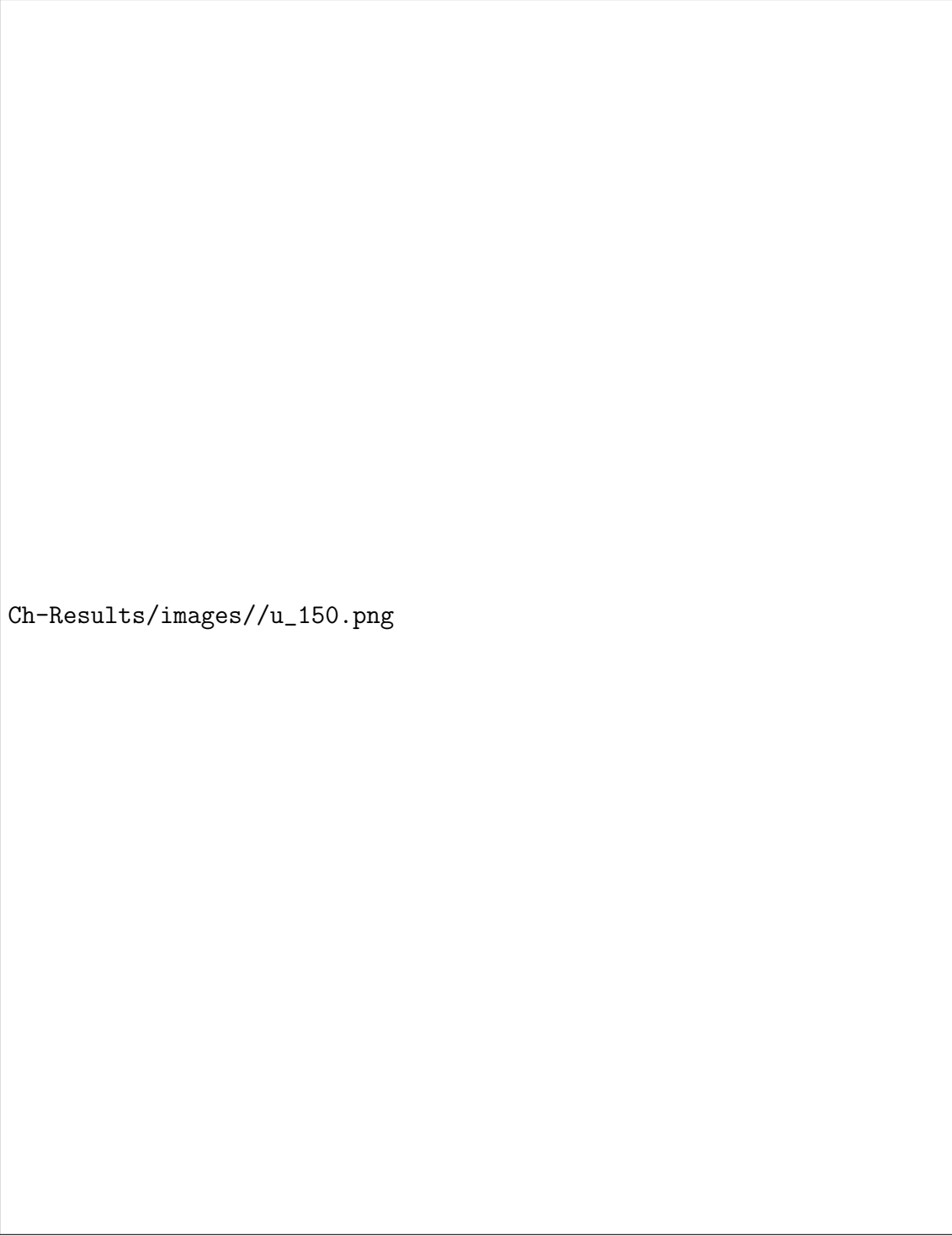
Figure 3.8: Root mean square error(RMSE) of the nozzle exit window using: s1 and s4 with studied time step  $\Delta t_1 = 2 \times 10^{-5}$ s,  $\Delta t_2 = 5 \times 10^{-5}$ s,  $\Delta t_3 = 10^{-4}$ s, mass flow rate,  $\dot{m} = 0.005$ lb/s, mode number,  $N = 150$ .

### 3.3.3.2 Sensitivity Analysis for Number of Dominant Modes

We used time-delay embedding along with sorting criteria for profile data( $n=263$ ). Since it contains velocity and pressure data across a line only (at exit nozzle) the rows of full order matrix contains makes insufficient number of elements (4 full periods and with the largest time step we will require 420 snapshots ( $m=480$ ,  $n < m$ )). To satisfy the condition we used 400times time delay embedding and created Hankel matrix of rows,  $n = 105200$ . Based on time sensitivity analysis we have chosen the time-step  $\Delta t_2=5 \times 10^{-5}$ s and took 6 periods for reconstruction and next 6 period for

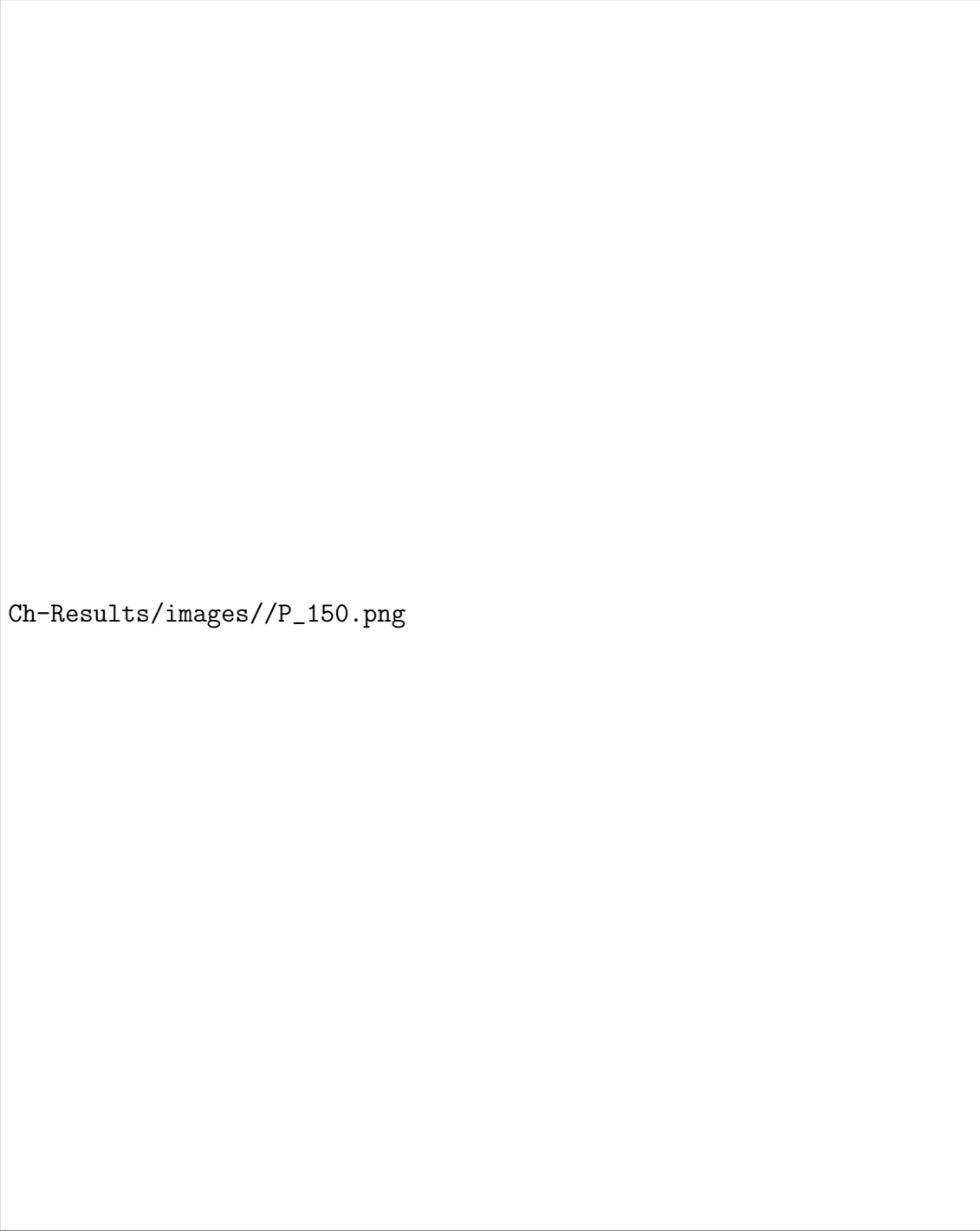


prediction. For this study we choose the maximum frequency system ( $f=131.75\text{Hz}$  and  $\dot{m}=0.005\text{lb/s}$ ). To choose desired number of modes we used two different modes ( $N=150/250$ ) which corresponds to 57% and 95% of total modes obtained from the data matrix decomposition. Our proposed algorithm performs better with time-delay embedding as well. (Fig. 3.9,3.10,3.11, 3.12). To study further we took the pressure and velocity probe sampling in very small scale (Fig. 3.13,3.14) and analyzed with only 5,10,20 modes which is 1.9%, 3.8%, 7.6% of our system rank. With only 40 modes sorting-4 can provide as much accuracy as with 150 modes in sorting-1. Reconstruction starts from the mean and subsequently captures the peaks of the oscillation. Since we kept the threshold of maximum absolute error within 12%. we selected mode,  $N=150$  for further study.



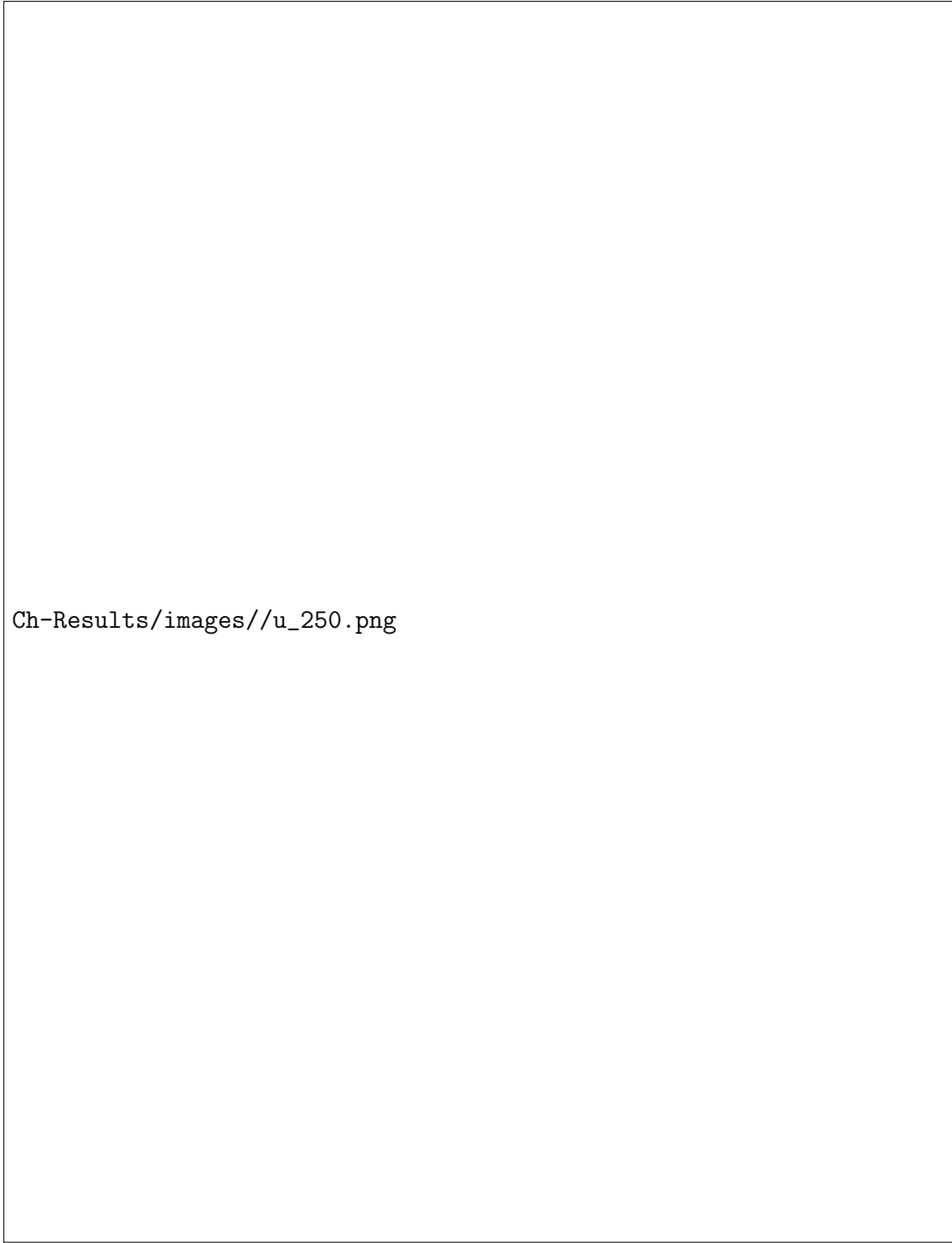
Ch-Results/images//u\_150.png

Figure 3.9: Velocity probe (0,0), 6 period of reconstruction s1 (S1) and s4 (S4) for  $\dot{m} = 0.005 \text{ lb/s}$ ,  $\Delta t = 5 \times 10^{-5} \text{ s}$ ,  $N = 150$ .  $u^*$  and  $t^*$  are normalized velocity and time period.



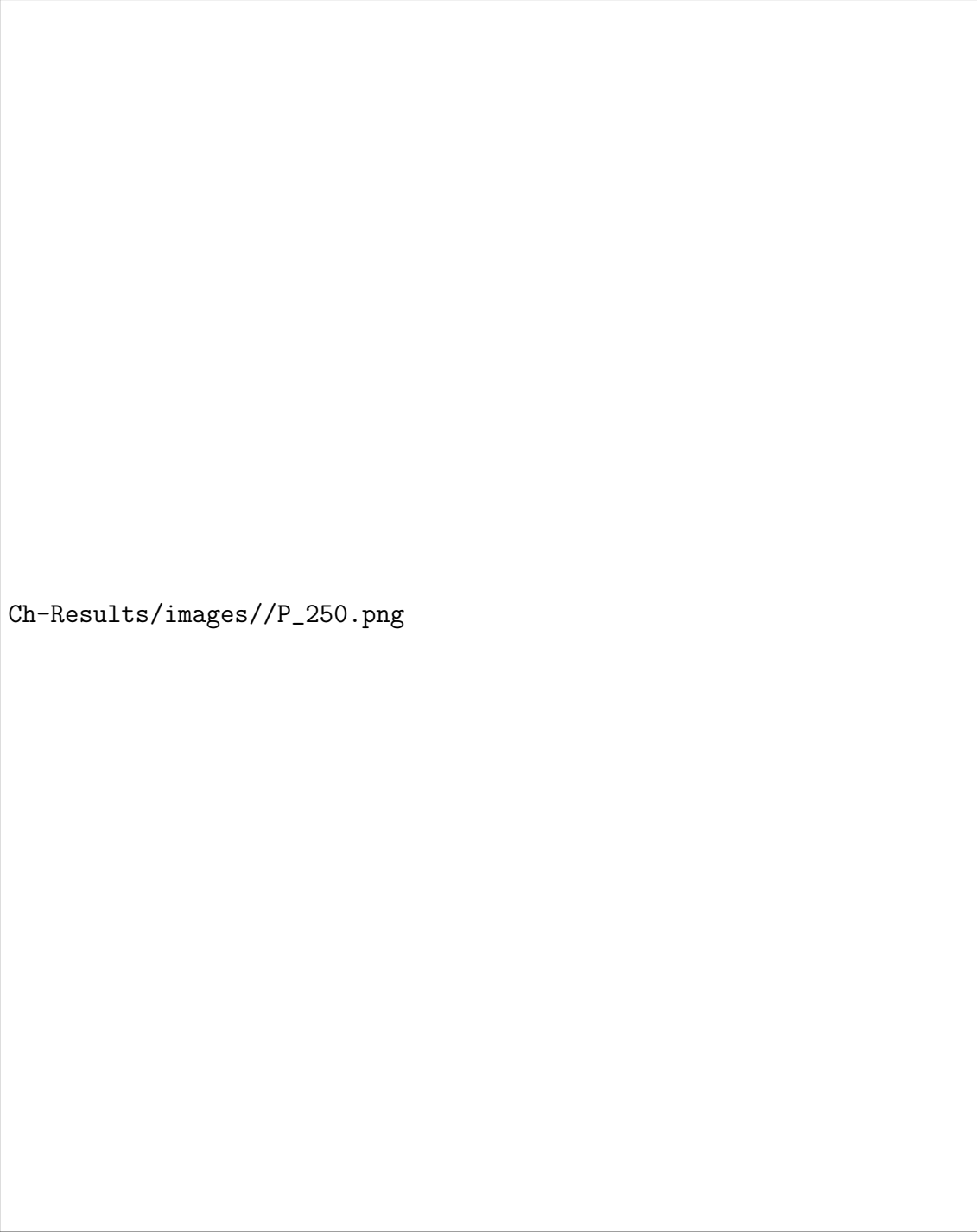
Ch-Results/images//P\_150.png

Figure 3.10: Pressure sub-sampling at center point (0,0), 6 periods of reconstruction  $s_1$  and  $s_4$  for  $\dot{m} = 0.005 \text{ lb/s}$ ,  $\Delta t = 5 \times 10^{-5} \text{ s}$ ,  $N = 150$ .  $P^*$  and  $t^*$  are normalized total pressure and time period.



Ch-Results/images//u\_250.png

Figure 3.11: Velocity sub-sampling at center point (0,0), 6 periods of reconstruction and another 6 periods of prediction with sorting-1 (S1) and sorting-4 (S4) for  $\dot{m} = 0.005 \text{ lb/s}$ ,  $\Delta t = 5 \times 10^{-5} \text{ s}$ ,  $N = 250$ .



Ch-Results/images//P\_250.png

Figure 3.12: Pressure probe at (0,0), 6 periods of reconstruction and 6 periods of prediction with s1 (S1) and s4 (S4) for  $\dot{m} = 0.005 \text{ lb/s}$ ,  $\Delta t = 5 \times 10^{-5} \text{ s}$ ,  $N = 250$ .

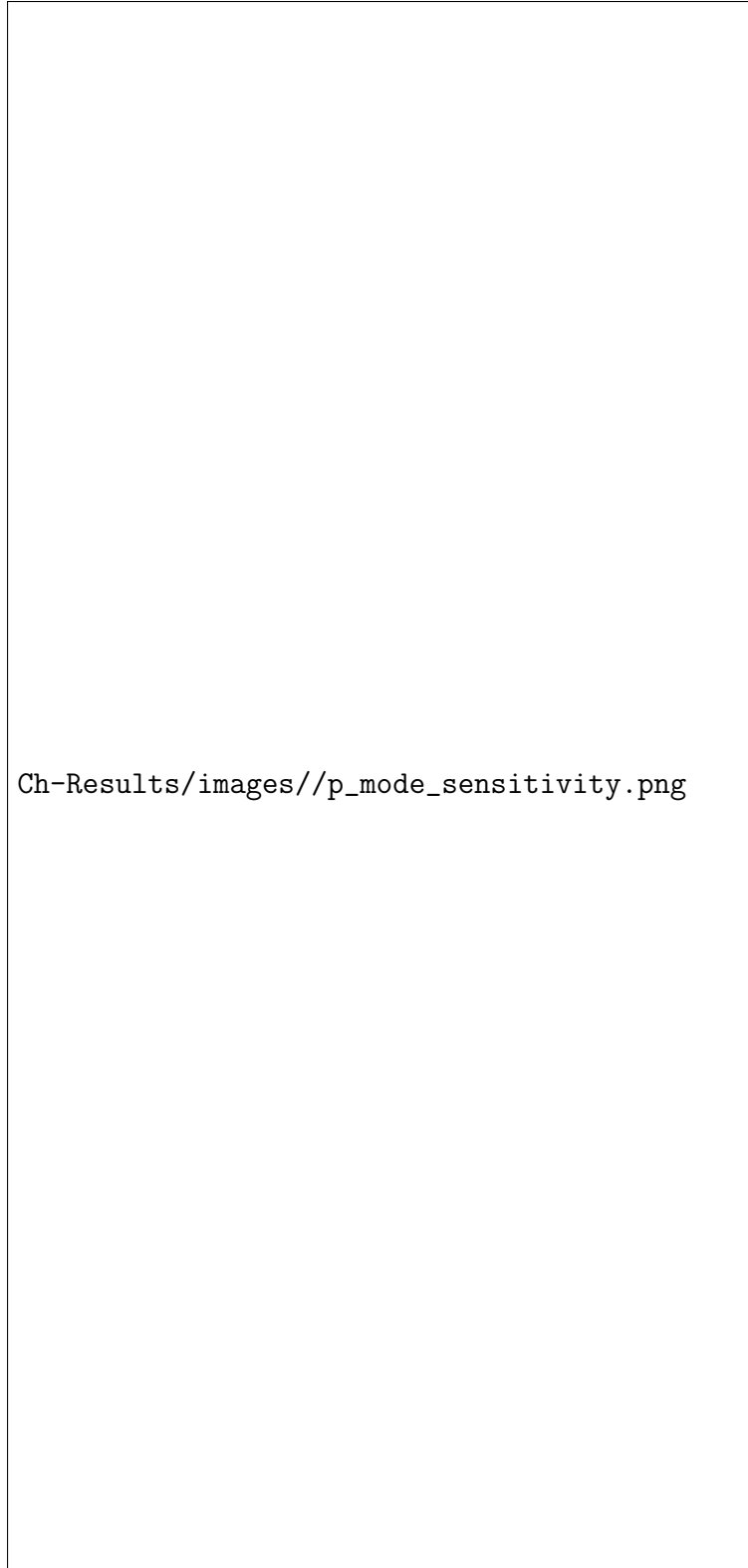


Figure 3.13: Pressure probe at (0,0) for low rank,m construction with s4: (a) N=5, (b) N=10, (c) N=20 for mass flow rate,  $\dot{m}=0.005\text{lb/s}$ ,  $\Delta t= 5\times 10^{-5}\text{s}$ .



Figure 3.14:  $u$ -velocity at centerpoint  $(0,0)$  for low rank(modes,m) construction with s4: (a)  $N=5$ , (b)  $N=10$ , (c)  $N=20$ .

### 3.3.3.3 Sensitivity Analysis for Oscillation Frequency

We studied for three different mass flow inlet,  $\dot{m}_1=0.0025\text{lb/s}$ ,  $\dot{m}_2=0.005\text{lb/s}$  and  $\dot{m}_3=0.01\text{lb/s}$  [2] corresponds to system frequency of 85.85Hz, 131.75Hz and 250.04Hz[10]. We focused on frequency 131.75Hz for detailed flow field analysis and boundary condition modeling. However, we verified the compatibility of our proposed algorithm for  $\dot{m}_1$  and  $\dot{m}_3$  as well (Fig. 3.15). For a low-frequency system, a smaller time-step is required to capture slower time dynamics (we showed the result for the minimum tested time-step) otherwise. it will cause overshooting at the initial stage since we have considered the amplitude for the second column snapshot ( $u_2$ ) instead of the first column. Due to this reason, slight overshooting can be seen in fig. 3.15(a). It can be resolved by taking smaller time steps. Since our focus is on higher frequency systems we showed that for 250.04Hz system frequency our algorithm can efficiently capture the reconstruction part and is quite aligned to the prediction phase as well (fig. 3.15(b)). We can use a larger time-step ( $\Delta t=10^{-4}\text{s}$ ) here reasonably because a smaller time-step might cause infinitesimally small motion making it difficult to capture time dynamics with fewer modes (affects the optimized setup).



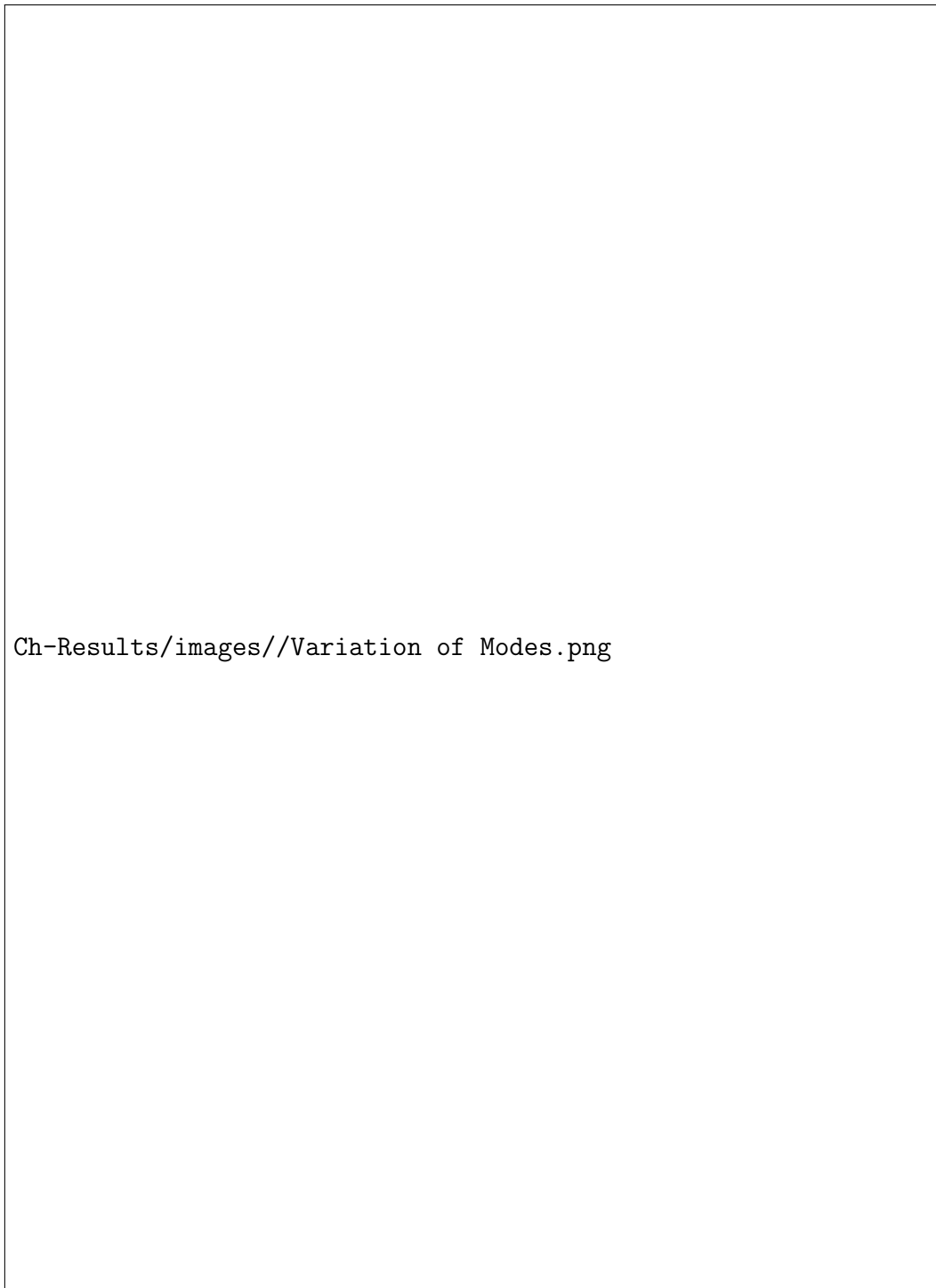


Figure 3.15: Point sampling (0,0) for u-velocity showing the reconstruction and prediction capability for (a)  $\dot{m}_1=0.0025\text{lb/s}$ ,  $\Delta t= 2\times 10^{-5}\text{s}$  and (b)  $\dot{m}_3=0.01\text{lb/s}$ ,  $\Delta t=10^{-4}\text{s}$  using s4.

### 3.4 Conclusion

The present study successfully demonstrates that the DMD algorithm can be employed in high-frequency oscillating systems such as Sweeping Jet Actuators. We further obtained low-rank profile reconstruction and prediction from this linear system that can be integrated with a larger domain for flow control applications. To summarize, we have deployed eigenvalue-based sorting to capture important features for the dynamics. For a high-resolution 2D flow field we have validated our model with 3 cycles of reconstruction data and 1 cycle of prediction. Our algorithm can preserve 88% of accuracy using only 31.25% of total modes. Point sampling at the center point shows the local performance of ES-DMD. Finally, we used 1D profile data and applied ES-DMD along with time-delay embedding which significantly improved the prediction phase using a very less number of modes ( $N=20$ , corresponds to 7.6% of total modes). For each particular case, ES-DMD shows a stable performance similar to CFD analysis. To address the limitation of linear surrogate modeling non-linear machine learning POD model is currently deployed to capture the recurrent pattern of the oscillation for a long period. For future work, obtained result will be employed in the full-scale wing model [94] to enable the practical effect of SJA in flow control elevating the burden of simulation or assumption of steady blowing [85].

## CHAPTER IV

### Remarks

#### 4.1 Summary

This thesis presents the research study at the Oklahoma State University focusing on the flow physics of Sweeping Jet Actuator. Computational fluid dynamics and reduced order modeling are used to analyze the flow domain. Since we are analyzing oscillating jet, it is an unsteady simulation with compressible flow. The aim is to accelerate the integration process in large scale models.

High fidelity model comprises iterative solution of the system governing equation. Time accuracy of the governing parameters are preserved with single time step, small enough to capture unsteady flow pattern in mean scale. SST  $k-\omega$  turbulent model provides the accuracy to model viscous sublayer near wall boundary region and provides the flexibility to simulate in freestream resolving the adverse pressure gradient and inlet freestream properties. For computational ease, 2D flow domain is considered to investigate the geometric variation at the exit nozzle. Studied parameter includes velocity, pressure, oscillation frequency, jet spread angle, mass flux at downstream of exit nozzle to discover the comparative performance of each geometry.

Based on velocity and pressure distribution on the flow topology, we took a sampling window around the exit nozzle region and sampled snapshots for various timesteps for data curation. Global data matrix is build from the snapshots where the spatial domain is flattened in each column and columns advancement represents the temporal scenario for the actuator domain. Since the oscillation is periodic decomposing the global matrix reduced the rank of system drastically by capturing only the dom-

inant modes to reconstruct the system without losing significant accuracy. Tailored mode selection is performed during the ROM development. The concluding remarks can be noted below: 2D CFD simulation is considered to analyze the fully turbulent actuator domain in quiescent environment resulting slight over prediction in the oscillation frequency for a given system compared to 3D analysis. This dissertation also validates that pressure sub-sampling provides robust oscillation frequency compared to velocity sampling. Realistic simulation to investigate the flow control efficiency of the SJA is required to simulate on the full wing with a couple of SJA. It has to be noted that the size of an SJA is significantly smaller than the size of a wing. This brings the issue of meshing to the table.

1. Oscillation frequency of Sweeping jet actuator is not effected by various shape of exit nozzle, rather it is dependent on internal geometry of the actuator[41].But curvature shape at exit nozzle increase downstream mass flux with coanda effect.
2. Jet spread at downstream increases if the nozzle length is smaller: facilitates better adhesion along the nozzle arms. Angle variation analysis shows that design optimization in selecting nozzle divergence can also play significant role in jet dispersion at downstream.Finally, direction of oscillating jet can be influenced by creating asymmetry in the nozzle length; longer arm guides the jet flow towards that direction.
3. Non-linear turbulent governing system can be modeled with simple linear equations having fewer DMD modes and 90% flow field accuracy can be recovered. Periodic oscillation can be captured with only 10% of the total dominant modes significantly eliminating the burden of computation. SJA domain stability depends on the growth rate of the system, emphasizing the dominance of positive eigenvalues to reconstruct the system.
4. Higher frequency oscillating system contains asymmetry in the local peaks resulting difficulty to capture the patterns in temporal dynamics. ES-DMD can successfully capture the local oscillating behaviour during the reconstruction but in prediction

phase fails to capture the local variation. On top of that, time-delay embedding can address this limitation and improves the model performance in the prediction phase as well.

5. ES-DMD provides the computationally efficient yet accurate model to establish SJA as a simple boundary condition instead of simulating the oscillating system, thus elevating the burden of meshing.

## 4.2 Limitations and Future Work

Based on thesis discussion, limitation and possible future work are as follows:

The research study is limited to 2D flow domain analysis assuming vortex shedding only evolves around x and y direction. In future, 3D full order CFD simulation can be performed on NASA trap wing model with high-lift configuration with detailed mesh independence test to validate the model[3]. For time-sensitivity dynamic mesh setup can be adopted to investigate unsteady flow separation behavior at the tailing edge of the aerodynamic wing. At the leading edge of the Trap wing SJA based DMD model can be integrated as a boundary condition to analyze the performance. Finally, validation of the results can be performed using this CFD simulation of the large scale SJA integrated wing model. Since application of DMD is limited to the reconstruction phase of the flow domain non-linear machine learning algorithm can resolve the issue.

## References

- [1] Surya Raghu. Fluidic oscillators for flow control. *Experiments in Fluids*, 54(2):1–11, 2013.
- [2] Kursat Kara. Numerical simulation of a sweeping jet actuator. In *34th AIAA Applied Aerodynamics Conference*, page 3261, 2016.
- [3] Mobashera Alam, Kursat Kara, and Aaron Alexander. Reduction of spanwise flow over a swept wing using an air curtain produced by rectangular slot. In *AIAA AVIATION 2022 Forum*, page 3296, 2022.
- [4] Nam-Hun Kim and Kwang-Yong Kim. Flow control using fluidic oscillators on an airfoil with a flap. *Engineering Applications of Computational Fluid Mechanics*, 15(1):377–390, 2021.
- [5] Kursat Kara, Daegyoun Kim, and Philip J Morris. Flow-separation control using sweeping jet actuator. *AIAA journal*, 56(11):4604–4613, 2018.
- [6] Mobashera Alam and Kursat Kara. The influence of exit nozzle geometry on sweeping jet actuator performance. *Fluids*, 7(2):69, 2022.
- [7] James W Gregory, John P Sullivan, and Surya Raghu. Visualization of jet mixing in a fluidic oscillator. *Journal of visualization*, 8(2):169–176, 2005.
- [8] Mehmet N Tomac and James Gregory. Frequency studies and scaling effects of jet interaction in a feedback-free fluidic oscillator. In *50th AIAA Aerospace Sciences Meeting including the New Horizons Forum and Aerospace Exposition*, page 1248, 2012.

- [9] Mehmet N Tomac and James Gregory. Jet interactions in a feedback-free fluidic oscillator at low flow rate. In *43rd AIAA Fluid Dynamics Conference*, page 2478, 2013.
- [10] Furkan Oz and Kursat Kara. Jet oscillation frequency characterization of a sweeping jet actuator. *Fluids*, 5(2):72, 2020.
- [11] Kursat Kara. Numerical study of internal flow structures in a sweeping jet actuator. In *33rd AIAA Applied Aerodynamics Conference*, page 2424, 2015.
- [12] Mehti Koklu. Effect of a coanda extension on the performance of a sweeping-jet actuator. *AIAA Journal*, 54(3):1131–1134, 2016.
- [13] Mehti Koklu and Lewis R Owens. Comparison of sweeping jet actuators with different flow-control techniques for flow-separation control. *AIAA Journal*, 55(3):848–860, 2017.
- [14] Mehti Koklu. Effects of sweeping jet actuator parameters on flow separation control. *AIAA Journal*, 56(1):100–110, 2018.
- [15] Shawn Aram and Hua Shan. Computational analysis of interaction of a sweeping jet with an attached crossflow. *AIAA Journal*, 57(2):682–695, 2019.
- [16] Brian T Bohan and Marc D Polanka. The effect of scale and working fluid on sweeping jet frequency and oscillation angle. *Journal of Fluids Engineering*, 142(6), 2020.
- [17] Louis N Cattafesta III and Mark Sheplak. Actuators for active flow control. *Annual Review of Fluid Mechanics*, 43:247–272, 2011.
- [18] Damian Hirsch and Morteza Gharib. Schlieren visualization and analysis of sweeping jet actuator dynamics. *AIAA Journal*, 56(8):2947–2960, 2018.

- [19] Célestin Ott, Quentin Gallas, Jérôme Delva, Marc Lippert, and Laurent Keirsbulck. High frequency characterization of a sweeping jet actuator. *Sensors and Actuators A: Physical*, 291:39–47, 2019.
- [20] Han-Sol Jeong and Kwang-Yong Kim. Shape optimization of a feedback-channel fluidic oscillator. *Engineering Applications of Computational Fluid Mechanics*, 12(1):169–181, 2018.
- [21] John C Lin, Edward A Whalen, Marlyn Y Andino, Emilio C Graff, Douglas S Lacy, Anthony E Washburn, Morteza Gharib, and Israel J Wygnanski. Full-scale testing of active flow control applied to a vertical tail. *Journal of Aircraft*, 56(4):1376–1386, 2019.
- [22] Tongil Park, Kursat Kara, and Daegyoun Kim. Flow structure and heat transfer of a sweeping jet impinging on a flat wall. *International Journal of Heat and Mass Transfer*, 124:920–928, 2018.
- [23] LaTunia G Pack Melton, John C Lin, Judith Hannon, Mehti Koklu, Marlyn Andino, and Keith B Paschal. Sweeping jet flow control on the simplified high-lift version of the common research model. In *AIAA Aviation 2019 Forum*, page 3726, 2019.
- [24] F Ostermann, R Wozidlo, CN Nayeri, and CO Paschereit. Interaction between a crossflow and a spatially oscillating jet at various angles. *AIAA Journal*, 58(6):2450–2461, 2020.
- [25] SangHoon Park, HeeChang Ko, MoonJung Kang, and Yeol Lee. Characteristics of a supersonic fluidic oscillator using design of experiment. *AIAA Journal*, 58(6):2784–2789, 2020.
- [26] Florian Ostermann, Rene Wozidlo, Christian Navid Nayeri, and Christian Oliver



- Paschereit. Properties of a sweeping jet emitted from a fluidic oscillator. *10.14279/depositonce-7144*, 2018.
- [27] Florian Ostermann, Philipp Godbersen, Rene Woszidlo, C Navid Nayeri, and C Oliver Paschereit. Sweeping jet from a fluidic oscillator in crossflow. *Physical Review Fluids*, 2(9):090512, 2017.
- [28] Hanns-Joachim Schmidt, Rene Woszidlo, Christian Nayeri, and Christian O Paschereit. Fluidic oscillators for bluff body drag reduction in water. In *54th AIAA Aerospace Sciences Meeting*, page 0591, 2016.
- [29] H-J Schmidt, R Woszidlo, CN Nayeri, and CO Paschereit. Separation control with fluidic oscillators in water. *Experiments in Fluids*, 58(8):1–17, 2017.
- [30] Amrit Adhikari, Thorge Schweitzer, Finn Lückoff, and Kilian Oberleithner. Design of a fluidic actuator with independent frequency and amplitude modulation for control of swirl flame dynamics. *Fluids*, 6(3):128, 2021.
- [31] Mahdi Nili-Ahmadabadi, Dae-Seung Cho, and Kyung Chun Kim. Design of a novel vortex-based feedback fluidic oscillator with numerical evaluation. *Engineering Applications of Computational Fluid Mechanics*, 14(1):1302–1324, 2020.
- [32] Masoud Alikhassi, Mahdi Nili-Ahmadabadi, Reza Tikani, and Mohammad Hassan Karimi. A novel approach for energy harvesting from feedback fluidic oscillator. *International Journal of Precision Engineering and Manufacturing-Green Technology*, 6(4):769–778, 2019.
- [33] Gabrielle C Claus, Andrew Hatton, Brian T Bohan, and Marc D Polanka. Internal geometry and external wall effects on fluidic oscillator behavior. *Journal of Fluids Engineering*, 142(11), 2020.

- [34] EI Dauengauer and RI Mullyadzhanov. Dynamics of fluidic oscillator jet: Les study. In *Journal of Physics: Conference Series*, volume 1382, page 012006. IOP Publishing, 2019.
- [35] Mohammad A Hossain, Robin Prenter, Ryan K Lundgreen, Ali Ameri, James W Gregory, and Jeffrey P Bons. Experimental and numerical investigation of sweeping jet film cooling. *Journal of Turbomachinery*, 140(3), 2018.
- [36] Xin Wen, Ziyang Li, Luanliang Zhou, Chengji Yu, Zubair Muhammad, Yudan Liu, Shiqi Wang, and Yingzheng Liu. Flow dynamics of a fluidic oscillator with internal geometry variations. *Physics of Fluids*, 32(7):075111, 2020.
- [37] Zongrui Hao, Gang Liu, Yue Wang, and Wanlong Ren. Studies on the drive mechanism of the main jet deflection inside a fluidic oscillator. *Industrial & Engineering Chemistry Research*, 59(20):9629–9641, 2020.
- [38] Mehmet N Tomac and Elias Sundström. Fluidic oscillator with variable sweep and inclination angles. *AIAA Journal*, 58(3):1182–1193, 2020.
- [39] Mehmet N Tomac and James W Gregory. Phase-synchronized fluidic oscillator pair. *AIAA Journal*, 57(2):670–681, 2019.
- [40] Mehmet N Tomac and Elias Sundström. Adjustable frequency fluidic oscillator with supermode frequency. *AIAA Journal*, 57(8):3349–3359, 2019.
- [41] Abdul Raouf Tajik, Kursat Kara, and Vladimir Parezanović. Sensitivity of a fluidic oscillator to modifications of feedback channel and mixing chamber geometry. *Experiments in Fluids*, 62(12):1–19, 2021.
- [42] Jeonglae Kim, Parviz Moin, and Avraham Seifert. Large-eddy simulation-based characterization of suction and oscillatory blowing fluidic actuator. *AIAA journal*, 55(8):2566–2579, 2017.

- [43] JG Zheng, L Xia, J Hu, and YJ Mao. Numerical investigation of characteristics of fluidic oscillator operating in quiescent air and a crossflow. *Aerospace Science and Technology*, 113:106731, 2021.
- [44] Jeffrey Slotnick, Judi Hannon, and Mark Chaffin. Overview of the 1st aiaa cfd high lift prediction workshop. In *49th AIAA Aerospace Sciences Meeting including the New Horizons Forum and Aerospace Exposition*, page 862, 2011.
- [45] Catherine McGinley, Luther Jenkins, Ralph Watson, and Arild Bertelrud. 3-d high-lift flow-physics experiment-transition measurements. In *35th AIAA Fluid Dynamics Conference and Exhibit*, page 5148, 2005.
- [46] Pierluigi Della Vecchia and Danilo Ciliberti. Numerical aerodynamic analysis on a trapezoidal wing with high lift devices: a comparison with experimental data. In *Paper presented XXII AIDAA Conference. AIDAA*, 2013.
- [47] KBMQ Zaman, Amy F Fagan, and Mina R Mankbadi. An experimental study and database for tip vortex flow from an airfoil. *NASA Report No. 20180000918*, 2017.
- [48] Prashanth Shankara and Deryl Snyder. Numerical simulation of high lift trap wing using star-ccm+. In *30th AIAA Applied Aerodynamics Conference*, page 2920, 2012.
- [49] Rob Ives, Stewart Keir, Edet Bassey, and Faik A Hamad. Investigation of the flow around an aircraft wing of section naca 2412 utilising ansys fluent. *INCAS Bulletin*, 10(1):95–104, 2018.
- [50] David M. Holman, Ruddy Brionnaud, Francisco Martinez, and Monica De Mier. Advanced aerodynamic analysis of the nasa high-lift trap wing with a moving flap configuration. In *30th AIAA applied aerodynamics conference*, page 2923, 2012.

- [51] Clarence W Rowley, Igor Mezić, Shervin Bagheri, Philipp Schlatter, and Dan S Henningson. Spectral analysis of nonlinear flows. *Journal of fluid mechanics*, 641:115–127, 2009.
- [52] Peter J Schmid. Dynamic mode decomposition of numerical and experimental data. *Journal of fluid mechanics*, 656:5–28, 2010.
- [53] Peter J Schmid and J Sesterhenn. Dynamic mode decomposition of experimental data. In *8th International Symposium on Particle Image Velocimetry, Melbourne, Victoria, Australia*, 2009.
- [54] Nail K Yamaleev, Mark H Carpenter, and Frederick Ferguson. Reduced-order model for efficient simulation of synthetic jet actuators. *AIAA journal*, 43(2):357–369, 2005.
- [55] Mihailo R Jovanović, Peter J Schmid, and Joseph W Nichols. Sparsity-promoting dynamic mode decomposition. *Physics of Fluids*, 26(2):024103, 2014.
- [56] Daniel F Gomez, Francis Lagor, Phillip B Kirk, Andrew Lind, Anya R Jones, and Derek A Paley. Unsteady dmd-based flow field estimation from embedded pressure sensors in an actuated airfoil. In *AIAA Scitech 2019 Forum*, page 0346, 2019.
- [57] Bernd R Noack, Witold Stankiewicz, Marek Morzyński, and Peter J Schmid. Recursive dynamic mode decomposition of transient and post-transient wake flows. *Journal of Fluid Mechanics*, 809:843–872, 2016.
- [58] Zhao Wu, Dominique Laurence, Sergey Utyuzhnikov, and Imran Afgan. Proper orthogonal decomposition and dynamic mode decomposition of jet in channel crossflow. *Nuclear Engineering and Design*, 344:54–68, 2019.

- [59] N Benjamin Erichson, Lionel Mathelin, J Nathan Kutz, and Steven L Brunton. Randomized dynamic mode decomposition. *SIAM Journal on Applied Dynamical Systems*, 18(4):1867–1891, 2019.
- [60] Steven L Brunton, Jonathan H Tu, Ido Bright, and J Nathan Kutz. Compressive sensing and low-rank libraries for classification of bifurcation regimes in nonlinear dynamical systems. *SIAM Journal on Applied Dynamical Systems*, 13(4):1716–1732, 2014.
- [61] David C Wilcox et al. *Turbulence modeling for CFD*, volume 2. DCW industries La Canada, CA, 1998.
- [62] FLORIANR Menter. Zonal two equation kw turbulence models for aerodynamic flows. In *23rd fluid dynamics, plasmadynamics, and lasers conference*, page 2906, 1993.
- [63] UDF Manual. Ansys fluent 12.0. *Theory Guide*, 2009.
- [64] Bartosz J Slupski, Abdul Raouf Tajik, Vladimir B Parezanović, and Kursat Kara. On the impact of geometry scaling and mass flow rate on the frequency of a sweeping jet actuator. *FME Transactions*, 47(3):599–607, 2019.
- [65] Veer Vatsa, Mehti Koklu, and Israel Wygnanski. Numerical simulation of fluidic actuators for flow control applications. In *6th AIAA Flow control Conference*, page 3239, 2012.
- [66] Zhen-Hua Wan, Lin Zhou, Bo-Fu Wang, and De-Jun Sun. Dynamic mode decomposition of forced spatially developed transitional jets. *European Journal of Mechanics-B/Fluids*, 51:16–26, 2015.
- [67] Joshua L Proctor, Steven L Brunton, and J Nathan Kutz. Dynamic mode decomposition with control. *SIAM Journal on Applied Dynamical Systems*, 15(1):142–161, 2016.

- [68] Peter J Schmid. Dynamic mode decomposition and its variants. *Annual Review of Fluid Mechanics*, 54:225–254, 2022.
- [69] Shady Emad Ahmed, Pedram H Dabaghian, Omer San, Diana Alina Bistrrian, and Ionel M Navon. Dynamic mode decomposition with core sketch. *Physics of Fluids*, 2022.
- [70] Naoya Takeishi, Yoshinobu Kawahara, Yasuo Tabei, and Takehisa Yairi. Bayesian dynamic mode decomposition. In *IJCAI*, pages 2814–2821, 2017.
- [71] Matthew O Williams, Ioannis G Kevrekidis, and Clarence W Rowley. A data-driven approximation of the koopman operator: Extending dynamic mode decomposition. *Journal of Nonlinear Science*, 25(6):1307–1346, 2015.
- [72] Xin Wen and Yingzheng Liu. Lagrangian analysis of sweeping jets measured by time-resolved particle image velocimetry. *Experimental Thermal and Fluid Science*, 97:192–204, 2018.
- [73] L Xia, Y Hua, and JG Zheng. Numerical investigation of flow separation control over an airfoil using fluidic oscillator. *Physics of Fluids*, 33(6):065107, 2021.
- [74] Abdul Raouf Tajik and Vladimir Parezanović. Additive manufacturing impact on a fluidic oscillator with respect to surface roughness. *International Journal of Heat and Fluid Flow*, 97:109040, 2022.
- [75] Liaqat Hussain and Muhammad Mahabat Khan. Recent progress in flow control and heat transfer enhancement of impinging sweeping jets using double feedback fluidic oscillators: A review. *Journal of Heat Transfer*, 2022.
- [76] Jonathan H Tu. *Dynamic mode decomposition: Theory and applications*. PhD thesis, Princeton University, 2013.

- [77] Zhi-Xian Ye, Yi-Yang Jiang, Ze-Nan Tian, Shao-Chang Mo, Yuan-Qi Fang, Jian-Feng Zou, and Yao Zheng. Analysis of synthetic jet piv experiment based on dynamic mode decomposition. *International Journal of Modern Physics B*, 34(14n16):2040103, 2020.
- [78] Yuan Yuan, Kaiwen Zhou, Wenwu Zhou, Xin Wen, and Yingzheng Liu. Flow prediction using dynamic mode decomposition with time-delay embedding based on local measurement. *Physics of Fluids*, 33(9):095109, 2021.
- [79] Jonathan Toomey and Jeff D Eldredge. Numerical and experimental study of the fluid dynamics of a flapping wing with low order flexibility. *Physics of Fluids*, 20(7):073603, 2008.
- [80] Joongcheol Paik, Cristian Escauriaza, and Fotis Sotiropoulos. On the bimodal dynamics of the turbulent horseshoe vortex system in a wing-body junction. *Physics of Fluids*, 19(4):045107, 2007.
- [81] Daniel J Garmann, Miguel R Visbal, and Paul D Orkwis. Three-dimensional flow structure and aerodynamic loading on a revolving wing. *Physics of Fluids*, 25(3):034101, 2013.
- [82] Chuan He, Thomas Corke, and Mehul Patel. Numerical and experimental analysis of plasma flow control over a hump model. In *45th AIAA aerospace sciences meeting and exhibit*, page 935, 2007.
- [83] Neal A Harrison, Jason Anderson, Jon L Fleming, and Wing F Ng. Active flow control of a boundary layer-ingesting serpentine inlet diffuser. *Journal of Aircraft*, 50(1):262–271, 2013.
- [84] Sang Hyouk Kim and Hyun Dong Kim. Quantitative visualization of the three-dimensional flow structures of a sweeping jet. *Journal of Visualization*, 22(3):437–447, 2019.

- [85] Rolf Radespiel, Marco Burnazzi, M Casper, and P Scholz. Active flow control for high lift with steady blowing. *The Aeronautical Journal*, 120(1223):171–200, 2016.
- [86] Christopher L Rumsey, JP Slotnick, M Long, RA Stuever, and TR Wayman. Summary of the first aiaa cfd high-lift prediction workshop. *Journal of Aircraft*, 48(6):2068–2079, 2011.
- [87] D Veerasamy, AR Tajik, L Pastur, and V Parezanović. Effect of base blowing by a large-scale fluidic oscillator on the bistable wake behind a flat-back ahmed body. *Physics of Fluids*, 34(3):035115, 2022.
- [88] Tauha Irfan Khan, Abdul Raouf Tajik, and Vladimir Parezanovic. Drag reduction of a generic transport vehicle model using a fluidic oscillator. *International Journal of Thermofluids*, page 100180, 2022.
- [89] Shady E Ahmed, Omer San, Diana A Bistrrian, and Ionel M Navon. Sampling and resolution characteristics in reduced order models of shallow water equations: Intrusive vs nonintrusive. *International Journal for Numerical Methods in Fluids*, 92(8):992–1036, 2020.
- [90] Wei Zhang and Mingjun Wei. Model order reduction using dmd modes and adjoint dmd modes. In *8th AIAA Theoretical Fluid Mechanics Conference*, page 3482, 2017.
- [91] Shady E Ahmed, Omer San, Diana Bistrrian, and Ionel Navon. Sketching methods for dynamic mode decomposition in spherical shallow water equations. In *AIAA SCITECH 2022 Forum*, page 2325, 2022.
- [92] W Cazemier, RWCP Verstappen, and AEP Veldman. Proper orthogonal decomposition and low-dimensional models for driven cavity flows. *Physics of fluids*, 10(7):1685–1699, 1998.



- [93] Shuli Hong, Guoping Huang, Yuxuan Yang, and Zepeng Liu. Introduction of dmd method to study the dynamic structures of a three-dimensional centrifugal compressor with and without flow control. *Energies*, 11(11):3098, 2018.
- [94] Christopher L Rumsey and Jeffrey P Slotnick. Overview and summary of the second aiaa high-lift prediction workshop. *Journal of Aircraft*, 52(4):1006–1025, 2015.

VITA

MOBASHERA ALAM

Candidate for the Degree of

Master of Science

Thesis: COMPUTATIONAL ANALYSIS OF SWEEPING JET ACTUATOR  
USING DYNAMIC MODE DECOMPOSITION

Major Field: Mechanical and Aerospace Engineering

Biographical:

Education:

Completed the requirements for the degree of Master of Science with a major in Mechanical and Aerospace Engineering at Oklahoma State University in December 2022.

Completed the requirements for the degree of Bachelor of Science with a major in Mechanical Engineering at Bangladesh University of Engineering and Technology in April 2019.

Experience:

Loves rafting, photography and hiking.

Professional Affiliations:

Student Member AIAA, APS